Free-surface film flow over topography: full three-dimensional finite element solutions

S. VEREMIEIEV*[1], H.M. THOMPSON[2], and P.H. GASKELL[1]

[1]School of Engineering and Computing Sciences, Durham University, Durham, DH1 3LE, UK

[2]School of Mechanical Engineering, University of Leeds, Leeds, LS2 9JT,UK

August 18, 2015

Abstract

An efficient Bubnov-Galerkin finite element formulation is employed to solve the Navier-Stokes and continuity equations in three-dimensions for the case of surface-tension dominated film flow over substrate topography, with the free-surface location obtained using the method of spines. The computational challenges encountered are overcome by employing a direct parallel multi-frontal method in conjunction with memory-efficient out-of-core storage of matrix co-factors. Comparison is drawn with complementary computational and experimental results for low Reynolds number flow where they exist, and a range of new benchmark solutions provided. These, in turn, are compared with corresponding solutions, for non-zero Reynolds number, from a simplified model based on the long-wave approximation; the latter is shown to produce comparatively acceptable results for the free-surface disturbance experienced, when the underpinning formal restrictions on geometry and capillary number are not exceeded.

Keywords: liquid film flow, finite elements, topography, long-wave approximation, Navier-Stokes.

*Corresponding author: s.veremieiev@gmail.com

1 Introduction

Processes involving the motion of liquid films on various substrates are encountered across engineering, the sciences and technology, as reported in the recent comprehensive review by [1]. Examples from nature include the control of disease in plants, [2], and the redistribution of the liquid linings of respiratory systems, [3]. They form an important component across several industrial sectors, including the coating of papers and plastics in the inkjet and photographic industries, [4], heat exchanger and combustion chamber design, [5], [6], and the application of anti-reflective coatings, [7]. They are also crucial in the cooling of electronic devices, [8], and in the manufacture of micro-scale electronic components, for example in direct-write printing of circuits, [9], where the precise deposition of liquid films flowing over a distribution of functional topographic features (such as polymer light-emitting species on a screen) is vital to ensuring acceptable product quality and performance.

The ever-increasing requirements for predictable product and process properties has generated considerable interest in improving the understanding of complex free-surface film flows over topography. In many practically-important situations these requirements translate into the need for reliable film thickness control. This is often very difficult to achieve since free-surface disturbances induced by small-scale topography can result in film thickness non-uniformities that persist over length scales several orders of magnitude greater than the size of the topography itself, [10]; other related experimental investigations of note supporting this include those of [11, 12], [13], [8] and [14]. While well suited to studying the flow over isolated or periodically repeating topographical features, the routine use of experiments in the context of product and/or process design can prove prohibitive both cost and time wise; hence the recourse, over the last decade or so, to modelling approaches coupled with the efficient numerical solution of the associated governing equations.

From a consideration of the three-dimensional nature of the flows of interest and the disparity in length-scales encountered, the majority of models to emerge are based on application of the long-wave approximation which utilise the feature that the undisturbed asymptotic film thickness is small compared to the characteristic in-plane length scale. The additional neglect of inertia enables such flows to be represented either by a fourth order non-linear degenerate partial differential equation for the film thickness, or by a coupled set of second order equations for

the film thickness and pressure, [15], albeit with formal restriction to surface tension-dominated flows having small capillary number and for which the topography depth/height is small compared to the film thickness. These, so-called, lubrication equations have been used successfully to model thin film flows for a range of problems including flows with evaporation, [16], with surfactants, [17], in the presence of an electric field, [18], and for the case of rivulet formation, [19]. The influence of inertia can also be important in terms of the magnitude of the free-surface disturbances that form, [20], and beyond a critical Reynolds number from the point of view of flow stability, [21, 22].

Despite their proven usefulness, the above models lack the generality associated with solving the governing Navier-Stokes and continuity equations themselves, which are not restricted in terms of choice of film thickness, size of capillary number or topography depth/height; another constraint lifted is that topographical features with perfectly steep sides can be accommodated without the need for smoothing. As might be construed, there are very few such film flow solutions in the literature; the exceptions being boundary element solutions obtained for Stokes flow, as reported by [23] and [24] for flow over a small particle and a three-dimensional obstacle, respectively, and by [25, 26] for flow past hemispheriod-shaped obstacles with large free-surface disturbances. Latterly, [14] obtained solutions with inertia present for film flow over a bi-periodically repeating substrate using a Volume of Fluid algorithm to investigate pattern formation and mixing; see also the work of [27] which addresses the capillary flow problem of dynamic wetting as an interface forming process.

The remainder of the paper is organised as follows. The three-dimensional flow problems considered are described in Section 2, which includes the governing equation set, with the corresponding finite element formulation and method of solution described in Section 3. A series of results demonstrating the power and accuracy of the solution strategy adopted and the flow phenomena that are induced are provided in Section 4. Finally, conclusions are drawn in Section 5.

2 Problem specification

The problems considered are for the case of steady-state, gravity-driven, free-surface film flow down a planar substrate, inclined at an angle $\theta(\neq 0)$ to the horizontal, and containing hemi-

spheroid or trench like topographical features, see Figure 1, of height/depth S_0, streamwise diameter/length L_T and spanwise diameter/width W_T. The liquid is assumed to be incompressible and to have constant density, ρ, dynamic viscosity, μ, and surface tension, σ. The chosen Cartesian streamwise, X, spanwise, Y, and normal, Z, components of the coordinate vector, $\boldsymbol{X} = X\boldsymbol{i} + Y\boldsymbol{j} + Z\boldsymbol{k}$, are as indicated; $\boldsymbol{i}$, $\boldsymbol{j}$, $\boldsymbol{k}$ are the corresponding basis vectors of the coordinate system. The solution domain is bounded from below by the substrate, $Z = S(X, Y)$, from above by the free surface, $Z = F(X, Y)$, upstream and downstream by the inflow, $X = 0$, and outflow, $X = L_P$, planes, respectively, and to the left and right by the side planes at $Y = 0$ and $Y = W_P$. The film thickness, $H(X, Y)$, at any point in the (X, Y) plane is given by $H = F - S$. The resulting laminar flow is described by the Navier-Stokes and continuity equations, namely:

$$\rho \boldsymbol{U} \cdot \nabla \boldsymbol{U} = -\nabla P + \nabla \cdot \boldsymbol{T} + \rho \boldsymbol{G}, \tag{1}$$

$$\nabla \cdot \boldsymbol{U} = 0, \tag{2}$$

where $\boldsymbol{U} = U\boldsymbol{i} + V\boldsymbol{j} + W\boldsymbol{k}$ and P are the fluid velocity and gauge pressure, respectively; $\boldsymbol{T} = \mu\left(\nabla \boldsymbol{U} + (\nabla \boldsymbol{U})^T\right)$ is the viscous stress tensor, $\boldsymbol{G} = G_0(\sin\theta \boldsymbol{i} - \cos\theta \boldsymbol{k})$ is the acceleration due to gravity where G_0 is the standard gravity constant.

Taking the reference length scale in all directions to be the asymptotic, or fully developed, film thickness, H_0, and scaling the velocities by the free-surface (maximum) velocity apropos the classic Nusselt solution, [28], $U_0 = \rho G_0 H_0^2 \sin\theta / 2\mu$, and the pressure (stress tensor) by $P_0 = \mu U_0 / H_0$, equations (1) - (2) can be rewritten in non-dimensional form as:

$$\mathrm{Re} \boldsymbol{u} \cdot \nabla \boldsymbol{u} = -\nabla p + \nabla \cdot \boldsymbol{\tau} + \mathrm{St} \boldsymbol{g}, \tag{3}$$

$$\nabla \cdot \boldsymbol{u} = \boldsymbol{0}, \tag{4}$$

where $\boldsymbol{x} = x\boldsymbol{i} + y\boldsymbol{j} + z\boldsymbol{k}$, $\boldsymbol{u} = u\boldsymbol{i} + v\boldsymbol{j} + w\boldsymbol{k}$, p, $\boldsymbol{\tau}$ and $\boldsymbol{g} = \boldsymbol{G}/G_0$ are the non-dimensional coordinate, velocity, pressure, viscous stress tensor and gravity component, respectively; $\mathrm{Re} = \rho U_0 H_0 / \mu$ is the Reynolds number and $\mathrm{St} = \rho G_0 H_0^2 / \mu U_0 = 2/\sin\theta$ is the Stokes number.

The general problem definition is complete following the specification of appropriate no-slip, inflow/outflow, kinematic and free-surface normal and tangential stress boundary conditions,

see [29]:

$$\boldsymbol{u}|_{z=s} = 0, \tag{5}$$

$$h|_{x=0} = 1, \quad \boldsymbol{u}|_{x=0,l_p;y=0,w_p} = z\,(2-z)\,\boldsymbol{i}, \tag{6}$$

$$(\boldsymbol{n}\cdot\boldsymbol{u})\,|_{z=f} = 0, \tag{7}$$

$$-p|_{z=f} + (\boldsymbol{\tau}|_{z=f}\cdot\boldsymbol{n})\cdot\boldsymbol{n} = \frac{\kappa}{\mathrm{Ca}}, \tag{8}$$

$$(\boldsymbol{\tau}|_{z=f}\cdot\boldsymbol{n})\cdot\boldsymbol{t} = 0, \tag{9}$$

where h, s, f together with s_0, l_t, w_t, l_p and w_p correspond to their dimensional counterparts, $\boldsymbol{n} = \left(-\frac{\partial f}{\partial x}\boldsymbol{i} - \frac{\partial f}{\partial y}\boldsymbol{j} + \boldsymbol{k}\right)\cdot\left[\left(\frac{\partial f}{\partial x}\right)^2 + \left(\frac{\partial f}{\partial y}\right)^2 + 1\right]^{-1/2}$ is the unit normal vector pointing outward from the free surface, $\boldsymbol{t} = \left[\alpha_t\boldsymbol{i} + \beta_t\boldsymbol{j} + \left(\alpha_t\frac{\partial f}{\partial x} + \beta_t\frac{\partial f}{\partial y}\right)\boldsymbol{k}\right]\cdot\left[\alpha_t^2 + \beta_t^2 + \left(\alpha_t\frac{\partial f}{\partial x} + \beta_t\frac{\partial f}{\partial y}\right)^2\right]^{-1/2}$ is the unit vector tangential to the free surface, $\mathrm{Ca} = \mu U_0/\sigma$ is the capillary number and $\kappa = -\nabla\cdot\boldsymbol{n}$ is twice the mean curvature of the free surface that is taken to be positive when the surface is concave upwards; α_t and β_t are variables that define the direction of the tangent vector at any point in the tangent plane; thus equation (9) actually implies two boundary conditions.

The hemispheroid and trench like topographic features under consideration are prescribed as follows:

$$s_{hemispheroid}\,(x^*, y^*) = \begin{cases} 0, & \left(\frac{2x^*}{l_t}\right)^2 + \left(\frac{2y^*}{w_t}\right)^2 \geq 1, \\ s_0\sqrt{1 - \left(\frac{2x^*}{l_t}\right)^2 - \left(\frac{2y^*}{w_t}\right)^2}, & \left(\frac{2x^*}{l_t}\right)^2 + \left(\frac{2y^*}{w_t}\right)^2 < 1, \end{cases} \tag{10}$$

$$s_{trench}\,(x^*, y^*) = \begin{cases} 0, & (x^*, y^*) \in [-x_t, l_p - x_t]\times[-y_t, w_p - y_t] \setminus \left(-\frac{l_t}{2}, \frac{l_t}{2}\right)\times\left(-\frac{w_t}{2}, \frac{w_t}{2}\right), \\ -s_0, & (x^*, y^*) \in \left(-\frac{l_t}{2}, \frac{l_t}{2}\right)\times\left(-\frac{w_t}{2}, \frac{w_t}{2}\right), \end{cases} \tag{11}$$

where $s_0\,(= S_0/H_0)$ is the dimensionless height/depth, with $l_t\,(= L_T/H_0)$ and $w_t\,(= W_T/H_0)$ such that for a hemispheroid $l_t = w_t$ is its non-dimensional foot-print diameter; for a hemispherical obstacle $l_t = w_t = 2s_0$. For a trench l_t and w_t are its streamwise length and spanwise widths, respectively. For convenience the coordinate system is placed at the centre of the topography, $(x_t, y_t, 0)$, denoted as: $(x^*, y^*, z) = (X/H_0 - x_t, Y/H_0 - y_t, Z/H_0)$.

Furthermore, taking advantage of the spanwise symmetry of the hemispheroid and trench

topography facilitates the governing equation set being solved over half the solution domain only, by imposing the following boundary conditions at the symmetry plane:

$$\frac{\partial u}{\partial y}|_{y^*=0} = v|_{y^*=0} = \frac{\partial w}{\partial y}|_{y^*=0} = \frac{\partial p}{\partial y}|_{y^*=0} = \frac{\partial h}{\partial y}|_{y^*=0} = 0. \tag{12}$$

3 Finite element formulation

The full Navier-Stokes (N-S) system of equations, (3)-(4), subject to the boundary conditions, (5)-(9), are discretised using an appropriate FE formulation, a complicating feature being the free surface that is present, whose shape is not known *a priori*. In line with the underpinnings of the FE method, the unknown velocity, pressure and grid coordinate fields are expanded in terms of basis functions (alternatively known as interpolation functions, trial functions or shape functions):

$$\boldsymbol{u} = \sum_{i=1}^{n^i} \boldsymbol{u}_i \phi_i, \quad p = \sum_{j=1}^{n^j} p_j \psi_j, \quad \boldsymbol{x} = \sum_{i=1}^{n^i} \boldsymbol{x}_i \phi_i, \tag{13}$$

where $i \in [1, n^i]$, $j \in [1, n^j]$, $\boldsymbol{u}_i = u_i \boldsymbol{i} + v_i \boldsymbol{j} + w_i \boldsymbol{k}$, p_j and $\boldsymbol{x}_i = x_i \boldsymbol{i} + y_i \boldsymbol{j} + z_i \boldsymbol{k}$ are the unknown nodal values of the velocity, pressure and coordinate fields, respectively; n^i is the total number of $\boldsymbol{u}/\boldsymbol{x}$-nodes and n^j is the total number of p-nodes; ϕ_i are basis functions for $\boldsymbol{u}/\boldsymbol{x}$ and ψ_j are basis functions for p. A 'mixed-interpolation' formulation with linear basis functions for pressure and quadratic basis functions for velocities and mesh coordinates is used, see [30], that results in n^i and n^j being different. This type of interpolation, in contrast to 'equal-order-interpolation', satisfies the so called LBB stability condition, [31], [32], [33], and ensures the pressure field is not polluted by spurious nonphysical oscillations. The same second-order interpolation for velocities and coordinates is permitted, see [34], allowing second-order-accurate free-surface locations to be obtained for almost the same computational cost. Accordingly, V10/P4/X10 (10 $\boldsymbol{u}/\boldsymbol{x}$-nodes and 4 p-nodes) tetrahedral elements are used.

A popular Bubnov-Galerkin weighted residual formulation, that assumes the weightings or test functions to be the same as the basis functions, is employed for the discretisation of equations (3), (4) and (7); this formulation has been applied successfully to various incompressible capillary-pressure dominated fluid flow problems, see [35] and [36]. The momentum equation (3) is converted into a discretised system of algebraic equations by multiplying it with appro-

priate weighting functions, integrating over the computational domain, Ω, and transforming the result into a divergence form using equation (4), boundary conditions (7) - (9) and the divergence theorem:

$$\int_{\Omega} \left(\mathrm{Re}\boldsymbol{u}\cdot\nabla\boldsymbol{u} + \nabla p - \nabla\cdot\boldsymbol{\tau} - \mathrm{St}\boldsymbol{g}\right)\phi_i d\Omega$$

$$= \int_{\Omega}\Big[\left(-\mathrm{Re}\boldsymbol{u}\otimes\boldsymbol{u} - p\boldsymbol{I} + \boldsymbol{\tau}\right)\nabla\phi_i - \mathrm{St}\boldsymbol{g}\phi_i\Big]d\Omega - \frac{1}{\mathrm{Ca}}\int_f \kappa\boldsymbol{n}\phi_i df = \boldsymbol{0}, \tag{14}$$

where df is a surface area, $\boldsymbol{I}$ is the unity tensor and $\otimes$ denotes dyadic product of two vectors. Due to the presence of no-slip and specified inflow/outflow boundary conditions (5) and (6), the surface integral in (14) is non-zero at the free surface only and can be simplified using the surface divergence theorem, that lowers the order of spatial derivatives, and the well-known expression for surface gradient $\nabla_s\phi_i = \nabla\phi_i - \boldsymbol{n}\left(\boldsymbol{n}\cdot\nabla\phi_i\right)$, see [37]:

$$\int_f \kappa\boldsymbol{n}\phi_i df = -\int_f\Big[\nabla\phi_i - \boldsymbol{n}\left(\boldsymbol{n}\cdot\nabla\phi_i\right)\Big]df + \oint_R \boldsymbol{t}|_R\phi_i dR, \tag{15}$$

where dR is the arclength along R, the curve bounding the free surface, and $\boldsymbol{t}|_R$ is a unit vector along R, tangential to the free surface but normal to R. The integration over R in (15) can be omitted due to the inflow/outflow boundary condition (6).

In a similar way the Bubnov-Galerkin formulation is applied to obtain the discrete form of the continuity equation, (4):

$$\int_{\Omega}\nabla\cdot\boldsymbol{u}\psi_j d\Omega = 0. \tag{16}$$

The discrete form of the kinematic boundary condition, (7), used to obtain the free-surface location, is written as:

$$\int_f \left(\boldsymbol{n}\cdot\boldsymbol{u}\right)\phi_k df = 0, \tag{17}$$

for any free-surface $\boldsymbol{u}/\boldsymbol{x}$-node $k \in \left[1, n^k\right]$, where $n^k\,(< n^i)$ is the total number of free-surface nodes.

To complete the system of discrete equations (14), (16) and (17) the spine method, [38], an Arbitrary Lagrangian-Eulerian approach suitable for use with FE formulations of both steady and unsteady problems, [34, 39], is employed; for steady flow it relates the positions of mesh nodes, $\boldsymbol{x}_i$, to a set of free-surface parameters called spinal distances, h_k, that change iteratively

to satisfy the kinematic boundary condition, (7):

$$\boldsymbol{x}_i = \Delta_{i,k}\left(\boldsymbol{x}_k^b + h_k \boldsymbol{d}_k\right) = \boldsymbol{x}_i^b + \Delta_{i,k} h_k \boldsymbol{d}_i, \tag{18}$$

where $\boldsymbol{x}_k^b$ and $\boldsymbol{d}_k$ are the fixed base nodes and fixed direction vectors of the spines, respectively. Each moving mesh node lies on one and only one spine and has a fixed base node, $\boldsymbol{x}_i^b = \Delta_{i,k}\boldsymbol{x}_k^b$, and a fixed direction vector, $\boldsymbol{d}_i = \Delta_{i,k}\boldsymbol{d}_k$, where the position of a node along a particular spine is a prescribed fraction of the spine's total length, h_k. The Boolean matrix, $\Delta_{i,k}$, is defined as:

$$\Delta_{i,k} = \begin{cases} 1, \text{ if the global node } i \text{ lies on the spine } k, \\ 0, \text{ otherwise.} \end{cases} \tag{19}$$

4 Method of solution

4.1 Newton-Raphson linearisation

The Newton-Raphson method is used to linearise the system of discrete N-S equations (14), (16), (17) and (18):

$$\frac{\partial \boldsymbol{\mathcal{N}}}{\partial \boldsymbol{z}} \Delta \boldsymbol{z} = -\boldsymbol{\mathcal{N}} \tag{20}$$

where the global residual vector, $\boldsymbol{\mathcal{N}}$, global Jacobian matrix, $\frac{\partial \boldsymbol{\mathcal{N}}}{\partial \boldsymbol{z}}$, global solution vector, $\boldsymbol{z}$, and its corresponding increment vector, $\Delta\boldsymbol{z}$, are, respectively:

$$\boldsymbol{\mathcal{N}} = \begin{pmatrix} \boldsymbol{\mathcal{N}}_i^{mom} \\ \mathcal{N}_j^{cont} \\ \mathcal{N}_k^{kin} \end{pmatrix}, \ \frac{\partial \boldsymbol{\mathcal{N}}}{\partial \boldsymbol{z}} = \begin{pmatrix} \frac{\partial \boldsymbol{\mathcal{N}}_i^{mom}}{\partial \boldsymbol{u}_l} & \frac{\partial \boldsymbol{\mathcal{N}}_i^{mom}}{\partial p_j} & \frac{\partial \boldsymbol{\mathcal{N}}_i^{mom}}{\partial h_m} \\ \frac{\partial \mathcal{N}_j^{cont}}{\partial \boldsymbol{u}_l} & 0 & \frac{\partial \mathcal{N}_j^{cont}}{\partial h_m} \\ \frac{\partial \mathcal{N}_k^{kin}}{\partial \boldsymbol{u}_l} & 0 & \frac{\partial \mathcal{N}_k^{kin}}{\partial h_m} \end{pmatrix}, \ \boldsymbol{z} = \begin{pmatrix} \boldsymbol{u_i} \\ p_j \\ h_k \end{pmatrix}, \ \Delta\boldsymbol{z} = \begin{pmatrix} \Delta\boldsymbol{u_i} \\ \Delta p_j \\ \Delta h_k \end{pmatrix}. \tag{21}$$

The global Jacobian matrix, including the terms $\frac{\partial \boldsymbol{\mathcal{N}}}{\partial h_m}$, is calculated analytically, see [40] for further details. After the increments, $\Delta\boldsymbol{z}$, have been obtained the solution is updated as follows:

$$\widetilde{\boldsymbol{z}} = \boldsymbol{z} + \Delta\boldsymbol{z}, \tag{22}$$

with typically 2 to 3 iterations required to reduce the norm of the residual $\boldsymbol{\mathcal{N}}$ to below 10^{-6}.

The integrals, (14), (16) and (17), necessary to obtain the global residual vector and Jacobian

matrix, are calculated numerically in a local natural coordinate system, [41], using symmetric Gaussian quadrature with 7 and 24 integration points for free-surface triangular and volumetric tetrahedral elements, respectively, [40]. The no-slip and inflow/outflow boundary conditions, (5) and (6), are imposed by replacing the corresponding weighted residual momentum equations (14) with the desired velocity there. In the same way, the boundary condition of fully developed flow, $h|_{x=0} = 1$, equation (6), is imposed by replacing the corresponding weighted residual kinematic equations (17) with the desired spine value.

4.2 Multifrontal solver

The system of linear algebraic equations (20) is solved using a parallel multifrontal method, that is a variant of Gaussian elimination initially developed for indefinite sparse symmetric linear systems by [42] and then extended to unsymmetric matrices, [43]. The use of a direct solver is particularly well suited to solving the dense matrices arising from application of the spine method in the case of steady-state free-surface flows, [34]. Accordingly, a widely used and efficient parallel implementation of the method from the MUltifrontal Massively Parallel sparse direct Solver (MUMPS) is employed, which is written in Fortran 90 with a C interface and invokes the well-known memory distributed parallel message passing interface (MPI) protocol, [44], together with the BLAS, [45], BLACS, and ScaLAPACK, [46] libraries. Only a brief description of the multifrontal method and the MUMPS library is provided here; for a more detailed overview of the multifrontal method see [47], while for the MUMPS library see [48], [49] and [50].

The solution process of the multifrontal method comprises three steps:

(i) an analysis step (or symbolic factorisation step) that only considers the pattern of the global Jacobian matrix, $\frac{\partial \boldsymbol{\mathcal{N}}}{\partial \boldsymbol{z}}$, and builds the necessary data structures for numerical computations;

(ii) a numerical factorisation step that performs calculation and assembly of the global Jacobian matrix and building of the sparse factors (e.g., the elements of the lower triangular matrix $\boldsymbol{L}$ and upper triangular matrix $\boldsymbol{U}$, such that $\boldsymbol{LU} = \frac{\partial \boldsymbol{\mathcal{N}}}{\partial \boldsymbol{z}}$);

(iii) a solution step, consisting of forward elimination (solves $\boldsymbol{Ly} = -\boldsymbol{\mathcal{N}}$ for a temporary vector $\boldsymbol{y}$) and backward substitution (solves $\boldsymbol{U}\Delta\boldsymbol{z} = \boldsymbol{y}$ for the increment $\Delta\boldsymbol{z}$).

The first, analysis, step partitions the computational domain by computing an efficient elimination tree that is used later in the factorisation stage. The elimination tree can be considered as the smallest data structure representing dependencies between the operations required for factorisation, see [51]. The multifrontal method employs a generalised version of the elimination tree, referred to as an assembly tree by [42], to determine the assembly order in the multifrontal method. Here the analysis stage is performed using an efficient multilevel nested dissection algorithm available as a serial (METIS_NODEND routine in METIS) or parallel (ParMETIS_V3_NodeND routine in ParMETIS) implementation, see [52] or [53], respectively. This algorithm reduces the storage and computational requirements of sparse matrix factorization methods by up to an order of magnitude compared to other widely used algorithms, such as the multiple minimum degree approach; however, unlike the latter, its elimination trees are suited for parallel direct factorization, minimising the intercommunication cost.

The second, factorisation, step performs a succession of partial factorisations of small dense matrices called 'frontal matrices', that are associated with each node of the assembly tree created during the analysis step. Each frontal matrix is divided into two parts: (i) the factor block, also called the fully summed block, which corresponds to the variables which are factorised when the elimination algorithm processes the frontal matrix; (ii) the contribution block which corresponds to the variables which are updated when processing the frontal matrix. Once partial factorisation is complete, the contribution block is passed to the 'parent' node. When contributions from all 'children' are available on the 'parent' node, they are assembled (i.e. summed with the values contained in the frontal matrix of the parent), see [42, 43].

As to the solution step, for three-dimensional free-surface problems the multifrontal method requires a large amount of memory that can be much larger than the physical (in-core) memory available; in which case an out-of-core storage approach is preferable, see [54], one in which just the frontal matrices are held in main memory while the factors, which are accessed during the final solution step only, are held in direct-access files stored on the hard drive. This approach allows much larger problems to be considered and reduces memory usage significantly (by a factor 5 to 10 on 1 to 4 processors, and a factor around 2 on 16 to 128 processors). In a parallel computing context, increasing the number of processors, and therefore available physical memory, can help keep large frontal matrices in-core.

5 Results

The calculations for all of the results reported here-on-in were performed on a parallel computer with distributed memory architecture and fast switching. The machine possessed multiple hardware configurations; the one chosen had multiple nodes, each with 8 cores and 12Gb of in-core memory (1.5Gb/core). A no-back-up high speed temporary disk space of 114Tb and 3Gb/s was used to store the out-of-core cofactors. Because of the distributed nature of the architecture with relatively small in-core memory, the ParMETIS library was used in the analysis phase of the multifrontal solver and the host made to be idle in the factorization and solve phases; the latter prevents memory imbalance due to the global Jacobian matrix being stored in the memory of the host processor, the penalty being a slight decrease in parallel efficiency and speed-up.

Fluid flow trajectories $\boldsymbol{x}_s = x_s\boldsymbol{i} + y_s\boldsymbol{j} + z_s\boldsymbol{k}$ are found by integrating along the path lines:

$$\frac{dx_s}{u} = \frac{dy_s}{v} = \frac{dz_s}{w} \tag{23}$$

with starting positions located at points which highlight the flow; this is done accurately using the Matlab 7.9 *streamline* function.

For both topographical features, the Nusselt velocity and pressure profiles are chosen to be the initial approximations for the velocity and pressure respectively, while the initial approximation for the spine heights (free-surface location) is taken to be that of a flat free-surface profile:

$$\boldsymbol{u}_i = \frac{(z_i - s_i)(2 - z_i - s_i)}{(1 - s_i)^2}, \quad p_j = 2(1 - z_j)\cot\theta, \quad h_k = 1, \tag{24}$$

where $s_i = s(x_i, y_i)$ are the substrate grid nodes; these are fixed and form the base nodes. The corresponding direction vectors are normal to the substrate and can be found from the initial mesh approximation and the spine definition (18):

$$\boldsymbol{x}_i^b = x_i\boldsymbol{i} + y_i\boldsymbol{j} + s_i\boldsymbol{k}, \quad \boldsymbol{d}_i = (z_i - s_i)\,\boldsymbol{k}. \tag{25}$$

The initial and consequent mesh approximations are found via equation (18).

Finally, since steady-state analyses only are considered, the limits governing hydrodynamic

stability have to be borne in mind. It has been shown that in the case of two-dimensional, gravity-driven film flow down a flat inclined substrate, there exists a critical Reynolds number, Re_{crit}, beyond which the flow becomes unstable to long waves, see [55], a result that has been verified experimentally by [56] and [57]. The classical linear stability constraint for film flow over a planar substrate (see e.g. [58], [59]) yields:

$$\mathrm{Re}_{crit} = \frac{5}{4}\cot\theta. \tag{26}$$

Although experiments have revealed that the presence of topography can extend Re_{crit} beyond the limit prescribed by equation (26) (see e.g. [60]), all of the non-zero Reynolds problems considered in the present work adhere to the above conservative criterion. Accordingly, the inclination angles explored for flow over a hemispheroid are $\theta = 7^\circ$ ($\mathrm{St} \approx 16.4$) and 45° ($\mathrm{St} = 2\sqrt{2} \approx 2.8$) – the latter inclination angle is the one considered by [25] when obtaining their Stokes flow solutions; while for flow over a trench topography the inclination angles considered are $\theta = 7^\circ$ and 30° ($\mathrm{St} = 4$) – the latter is the one used in the experiments of [10]). Inclination angles of $\theta = 7^\circ$, 30° and 45° lead to $\mathrm{Re}_{crit} \approx 10.2$, 2.17 and 1.25, respectively. For $\theta = 7^\circ$ results are considered up to $\mathrm{Re} = 10$, when $\theta = 45^\circ$ for $\mathrm{Re} = 0$, while when $\theta = 30^\circ$ for $\mathrm{Re} \leq 2.45$ in light of the experiments of [10] who, incidentally, observed flow stability beyond this value.

5.1 Mesh independence and computational efficiency

A FE mesh structure was employed with a higher concentration of elements in the vicinity of the topography; see Figure 2 which shows the mesh structures adopted for each topography type after taking advantage of the symmetry present. For the problems of interest, the number of elements in the mesh was systematically increased until the maximum change in the predicted free-surface profiles on consecutive meshes became less than 0.05%, with mesh independency ensured for both the free-surface location and throughout the flow interior. The associated mesh involved subdivision of the solution domain using a total of $6 \times 80 \times 40 \times 8$ elements (spanning the entire substrate for $s \geq 0$) and $6 \times 20 \times 10 \times 16$ additional elements (within the trench, $s < 0$); note that parallelepipeds are divided into 6 tetrahedrons. Equivalently, for the hemispheroid (trench): the total number of elements $n^e = 153600(172800)$; the number of free-surface elements $n^s = 6400(6400)$; the number of $\boldsymbol{u}/\boldsymbol{x}$-nodes $n^i = 221697(249249)$, p-nodes

$n^j = 29889(33585)$ and free-surface $\boldsymbol{u}/\boldsymbol{x}$-nodes $n^k = 13041(13041)$; and the total number of degrees of freedom DOF $= 3n^i + n^j + n^k = 708021(794373)$.

Taking flow over a square trench (with $l_t = w_t = 3$, $s_0 = 1.0$, $l_p = w_p = 550$, $x_t = 195$, $y_t = 225$, Re $= 10$, Ca $= 0.001$ and $\theta = 7^\circ$) as a benchmark, Figures 3 and 4 confirm the above; they show profiles of the u, v and w velocity components passing through the centre of the trench in both the streamwise and spanwise directions as the total number of degrees of freedom DOF is increased. The former, Figure 3, are for velocity components at the free surface; the latter, Figure 4, are their values at the plane $z = 0$.

Figure 5 presents the related CPU time dependence on mesh density (when a different number of processors is used) and speed-up dependence on the number of processors (for two different problem sizes). The speed-up is expressed as the ratio of the execution time of the corresponding sequential algorithm on a single processor to the execution time for the parallel algorithm on multiple processors. In the case of a single processor a purely sequential version of MUMPS (together with BLAS and METIS) was used. As can be seen from Figure 5a the computational complexity of the algorithm is almost totally independent of the number of processors employed, with the number of operations required for the calculation being nearly linear in terms of the total number of degrees of freedom: $O(\text{DOF}^{1.25})$.

Figure 5b shows the parallel performance and scalability acheived, with better speed-up obtained for the coarse mesh problem, for which the total number of DOF $= 16413$. For the finer mesh problem, were the total number of DOF $= 108909$, a speed-up of 12.5 is accomplished consistent with and as expected for LU factorisation, see [61]. It is also evident that the speed-up can reasonably be expected to increase further as the number of processors is increased. Apart from the overhead from inter-processor communication, the inherent efficiency loss may be attributed to the relatively poor parallel scalability of the algorithm, which is more suited to the solution of sparse rather than dense matrices, as well as non-participation of the host in the calculations. Based on the above findings, all the N-S results discussed subsequently were obtained using 8 processors and an FE mesh having a total number of 708021(794373) DOF for flows containing a hemispheriod (trench) topography; while ensuring mesh independent solutions, enough in-core memory was guaranteed to be available to enable calculations to be completed in a matter of hours. Note also that the resulting N-S solutions are compared with their counterparts obtained using a simplified depth-averaged form (DAF) of equations

(3) and (4), akin to the integral boundary layer approach, [62, 63] and [64]; full details of the underpinning methodology can be found in [20], but for completeness the essential features are provided in Appendix A.

5.2 Film flow over a hemispheroid

Initially, solutions were obtained for Stokes flow over a hemispheric obstacle with diameter $l_t = 1.8$ ($w_t = 1.8$ and $s_0 = 0.9$) as considered by [25], enabling direct comparison with the predictions they achieved using a boundary element (BE) discretisation of the governing equations – see their Figures 15 and 16. The boundary element method has similarly been employed by [23] and [24] to investigate Stokes flow over three-dimensional obstacles but for cases of small free-surface deflections.

The substrate is inclined at $\theta = 45°$, the domain dimensions are $l_p = w_p = 100$ and the hemispheric obstacle is located at $(x_t, y_t) = (40, 50)$. Figure 6(a,c) compares free-surface profiles along the streamwise centreline for cases with Ca = 0.022 and 0.445 (B = 20 and 1 in the original paper, respectively), while Figure 6(e) shows the maximum and minimum free-surface disturbances, away from the planar value, for a range of Ca. In all cases the FE and BE predictions are seen to be in excellent agreement, exhibiting the same free-surface features and response to changing Ca. Shown also are the corresponding DAF predictions which are much less satisfactory, but this is only to be expected given the underpinning limitations governing its strict range of applicability.

The same flow problem was then solved for the case Re = 10; the N-S and DAF predictions obtained are shown in Figures 6(b), (d) and (f). Note that the substrate containing the topography is now inclined at an angle of $\theta = 7°$ to the horizontal in order to comply with the stability criterion given by (26). Re = 0 solutions are included as a reference point confirming, as expected, that the free-surfaces disturbances experienced are much smaller than when the substrate is inclined at $\theta = 45°$. It can be seen from the figures that increasing Re leads to a corresponding increase in the magnitude of the free-surface disturbances experienced, a result consistent with the findings of [65] for flow over a rectangular peak topography, as does an increase in Ca. An interesting observation from both sets of results is that while the DAF predictions are comparatively poor they tend to capture the minimum associated with

the downstream trough disturbance more satisfactorily, which is particularly so for the case $\mathrm{Re} = 10$.

Figure 7 presents fluid flow trajectories within and at the surface of the film, obtained by integrating along path lines with starting positions at $z = 0.4$ and $z = f$, for the same flow problem. The predicted flow patterns for $\mathrm{Re} = 0$, Figure 7(a,b), compare very well with the corresponding solution obtained by [25] – their Figure 14. In addition to showing the effect of changing Ca from 0.022 to 0.445 on the free-surface disturbance along the centre line only, as in Figure 6(b,d), it provides a more detailed picture of the global free-surface response and the change to the accompanying internal flow pattern. The effect of Ca on the latter is negligible other than close to the obstacle; this is more easily observed in Figure 7(e,f) which shows a view from above of the flow trajectories at $z = f$, moving from left to right. The flow patterns in Figure 7(c,d) are for the same two Ca values but when $\mathrm{Re} = 10$. It can be seen, when viewed in conjunction with Figure 7(e,f), that an increase in Re effectively displaces the trajectories downstream and that this effect is experienced throughout the flow, unlike when Ca alone is increased.

Figure 8 compares N-S and DAF predictions of the free-surface disturbance experienced by film flow over a hemispheroid for which, unlike the cases considered in Figures 6-7, the footprint diameter is large compared to its height ($l_t = w_t = 9.0$, $s_0 = 0.9$); in which case the geometry is expected to conform more suitably to the thin-film geometrical restrictions underpinning the DAF. It is clear that the DAF predictions are now much more in line with their N-S counterparts and capture the free-surface rise over the hemispheroid and the trough immediately downstream of it, even for the higher Ca value. Following [66] the error in the DAF predictions can be quantified in terms of the maximum discrepancy between the DAF and N-S predictions along the streamwise centreline; for the above case the errors are 3.7% and 2.7% for $\mathrm{Ca} = 0.022$ and 0.445, respectively. Figure 9 shows corresponding predictions for flow over a hemispheroid with a much smaller footprint ($l_t = w_t = 1.8$, $s_0 = 0.9$). In this case the geometry is less consistent with the underpinning thin-film assumptions; the result is that the agreement is generally poorer, with the maximum discrepancies between the N-S and DAF predictions increasing to 3.9% and 13.9% respectively.

5.3 Film flow over a square trench

Figure 10 shows the predicted free-surface disturbance experienced by a film flowing over the square trench topography studied experimentally by [10] with $l_t = w_t = 12$, $s_0 = 0.25$, Re $= 2.45$, Ca $= 3.5 \cdot 10^{-4}$ and $\theta = 30°$ (see Figure 7 of [10] for a corresponding colour plot). Only the N-S solution is shown, since its DAF counterpart is visually identical, revealing the upstream capillary ridge, downstream surge and bow wave features typical of such flows, [66]. Where they do differ is revealed in Figure 11 which shows the predicted streamwise and spanwise free-surface profiles at three different locations; superimposed on which is the experimental data of [10], see Figures 8 and 9 therein. As anticipated, at the relatively small Re and Ca values concerned, for which the usual thin film assumptions are expected to hold, the N-S and DAF solutions are in perfect agreement other than at the free-surface trough in the vicinity of the trench. Note, that although there is some noise in the free-surface profiles obtained experimentally, the r.m.s. difference observed between them and what is predicted is typically less than 1% of the depth of the trench. The steepness of the topography will influence the predicted free-surface profile around the trench: remembering that the FE method of solution can deal with trenches having perfectly steep sides, slightly better agreement is observed between the DAF predictions and experiment if the steepness parameter, see equation (34), associated with the topography appearing explicitly in the depth-averaged equation set, is increased from $\delta = 0.001$ to 0.05, the value used by [66]. This suggests, as might be expected, that the trench topography used in the experiments was neither perfectly steep nor had sharp 90° corners.

While the above numerical results for flow over a trench topography are encouraging in relation to the DAF and predicted free-surface behaviour, the same are expected to become increasingly inaccurate as each of the Re, Ca and topography size are increased, [20]. Figure 12 demonstrates the effect of increasing Ca over a wide range, from 0.001 to 0.1 (such a range can be achieved by varying the film thickness, for example), for flow past the trench topography considered by [10] with $l_t = w_t = 12$ and $s_0 = 0.25$ but now with Re $= 0$ and $\theta = 7°$. The N-S results show that increasing the capillary number increases the free-surface disturbance away from planarity (observed for Ca $= 0$); the disturbance becomes more pronounced and deeper and more closely conforms to the topography shape, a finding that is consistent with the results of [67] for 2-D Stokes flow over a trench – see Figures 3, 4 and 7 therein. Compared to the

free-surface N-S solutions shown, the DAF is found to slightly over-predict the magnitudes of the capillary ridge, surge and depression; following [20], the maximum error, compared to the corresponding N-S solution, is 0.4%, 0.9% and 1.8% for Ca = 0.001, 0.01 and 0.1, respectively. Even so, this demonstrates that the DAF predictions can be considered sufficiently accurate even when Ca = 0.1.

Figure 13 shows the corresponding predictions for inertial flow with Re = 10; increasing Ca leads to enhanced free-surface disturbances and greater conformity with the underlying trench topography. The maximum errors associated with the DAF compared to the N-S solutions are again found to be reasonably small, having values 0.8%, 1.2% and 3.3% for Ca = 0.001, 0.01 and 0.1, respectively. These results confirm those for film flow over a hemispheroid investigated above, in that an increase Ca while exacerbating the free-surface disturbance in the vicinity of the topography, the effect is less so than when Re is increased and in addition the consequence of the latter is felt away from the topography itself.

As for the case of film flow over a hemispheriod, Figure 14 presents fluid flow trajectories within and at the surface of the film, obtained by integrating along path lines with starting positions at $z = 0.05$ and $z = f$. In addition to showing the effect of changing Ca from 0.001 to 0.1 on the free-surface disturbance along the centre line only, as in Figure 12(b,e), it provides a more detailed picture of the global free-surface response and accompanying change to the internal flow pattern. Since the streamwise and spanwise extents of the trench ($l_t = w_t = 12$) are quite large compared to its depth ($s_0 = 0.25$) the flow remains essentially streamwise across the bulk of the trench – the geometry is such that the flow does not form a large-scale eddy structure within the trench itself. This is easily confirmed by exploring flow trajectories with starting position at $0.05 < z < f$. For a trench geometry such as this, any eddies that do form would normally be expected to be small and reside in the vicinity of its base corners, [68]. The flow is seen to enter the trench from both the upstream and the spanwise sides and to exit from the downstream side which leads to the associated capillary surge, agreeing with the interpretation given by [66]. The effect of Ca on the flow trajectories is negligible other than at the spanwise entrance into the trench; this is more easily observed in Figure 14(e,f) which provides a view from above of the flow trajectories at the free surface which are from left to right. The flow trajectories in Figure 14(c,d) are for the same two Ca values but when Re = 10. It can be seen, when viewed in conjunction with Figure 14(e,f), that an increase in Re has a

similar effect to the one experienced by film flow over a hemispheriod: it effectively straightens and displaces the trajectories downstream.

The final set of results, shown in Figure 15, considers the performance of the DAF relative to corresponding N-S solutions for the case of flow over a deeper trench topography, having $l_t = w_t = 12$, $s_0 = 1.0$, Re $= 0$ and $\theta = 7°$. Since the free-surface disturbance is more pronounced and deeper for such a trench the relative performance of the DAF is much worse (the same finding was observed for step-up and step-down topographies by [20]) especially for the higher Ca values: the maximum errors compared to the N-S predictions being 3.4%, 7.1% and 14.0% for Ca = 0.001, 0.01 and 0.1 respectively. These errors would be larger still if the depth of the trench remained at 1.0 and Re was increased to 10.

6 Conclusions

The problem formulation and method of solution presented are found to be well suited to the investigation of film flow over topography requiring a simultaneous understanding of the underpinning three-dimensional flow structure and free-surface disturbance experienced. The latter is important in the context of reliable film thickness control in many practically-relevant flows, while the former has an important influence on heat and mass transfer processes in many engineering and industrial flow systems, [69]. Accordingly, it marks a step forward from utilising equation sets resulting from application of the long-wave approximation to the governing continuity and Naver-Stokes equations, which offer solution simplicity at the expense of ignoring the internal flow. Similarly, it overcomes the constraints of small capillary number, topography steepness and film thickness limits restricting the range of applicability of such models. The computational challenges involved in exploring such free-surface problems based on solving the full Navier-Stokes and continuity equations are, however, considerable and is arguably the reason why the results reported above are the first of their kind.

For the problems investigated care has been taken to ensure the mesh independence of solutions while in tandem the efficiency of the parallel solution strategy has been explored – although not optimal, it was never the intention to pursue this, it can be explained in terms of a lack of parallel scalability of the algorithm, overheads from inter-processor communications as well as non-participation of the host in the calculations. In the absence of any experimental

data with which to compare, other than that of [10] for flow over trench like topography, comparisons are drawn with results for related Stokes flow problems available in the literature - namely flow over a hemispheroid as investigated by [25]. In all cases it is ensured that the flow does not violate, the arguably conservative, classical stability criterion for gravity-driven film flow down an inclined plane.

For the case of film flow over hemispheriods, the predictions obtained using the N-S solver are shown to produce results in excellent agreement with those of [25] for Stokes flow at different capillary numbers, in terms of both the free-surface disturbance and underpinning internal flow. Introducing inertia reveals that the same has a greater influence on both the free surface and internal flow, in that in the case of the latter it does not remain local to the topography as in the case of increasing capillary number. The same problems are solved using the simpler DAF equation set but with much less success; while the DAF captures the gross free-surface features the errors involved are large, which is only to be expected given that all of the assumptions underpinning it are severely compromised.

The second problem to be explored in detail is that of flow over trench topography in which it is found that both the N-S solver and solution of the DAF capture almost identically the free-surface disturbance experienced by the flow explored experimentally by [10]; for this problem the trench geometry and flow parameters are more in keeping with the long-wave approximation and as such good agreement is observed between the two set of results, despite the fact the topography steepness is captured exactly within the finite element formulation, while in the depth-averaged equation set it has to be encapsulated explicitly in an approximate fashion. This is an interesting feature in itself in that it suggests, based on the disagreement between the predictions and experiment apropos the free-surface trough experienced, the trench used in the experiments may not have been as steep-sided or have corners as sharp as anticipated. As in the case of flow over a hemispheroid topography, the introduction of inertia leads to an increasing disparity, for the same reasons, between the two sets of predictions; narrowing the trench improves matters but making the same deeper has the opposite effect - widening such a narrow deep trench would make the disparity between them greater still. The combined flow structure and free-surface plots show that increasing inertia similarly straightens the associated flow trajectories downstream.

While being clearly valuable in their own right, the results as reported are extremely encour-

aging and lead the way to obtaining an even better understanding of the accompanying internal flow structure involved, as in the case of the idealised two-dimensional film flow investigated by [70]. Just such an investigation of the eddy patterns present in trench topography, as its aspect ratio and the flow Reynolds number are varied, is underway. In addition, provided the underpinning assumptions related to the topographical features over which the film flows are not violated, the DAF appears able to adequately predict the associated free-surface disturbance when the capillary number involved is larger than that for which the method is strictly valid.

Appendix A

Depth-Averaged Form (DAF) and Method of Solution

Equations (3) and (4) with attendant boundary conditions (5) to (9) can be reformulated and simplified using the so-called long-wave approximation based on the assumption that $\varepsilon = H_0/L_0 \ll 1$, where L_0 is the characteristic in-plane capillary length scale, $L_0 = H_0/\left(6\mathrm{Ca}\right)^{1/3}$, and which is strictly valid only for the case of small capillary number, $\mathrm{Ca} = \varepsilon^3/6 \ll 1$. Averaging across the depth of the film results in the following equations, see [20] for further details:

$$\frac{6}{5}\mathrm{Re}\left(\bar{u}\frac{\partial \bar{u}}{\partial x} + \bar{v}\frac{\partial \bar{u}}{\partial y}\right) = -\frac{\partial p}{\partial x} - \frac{3\bar{u}}{h^2} + 2, \tag{27}$$

$$\frac{6}{5}\mathrm{Re}\left(\bar{u}\frac{\partial \bar{v}}{\partial x} + \bar{v}\frac{\partial \bar{v}}{\partial y}\right) = -\frac{\partial p}{\partial y} - \frac{3\bar{v}}{h^2}, \tag{28}$$

$$p = -\frac{1}{\mathrm{Ca}}\nabla^2\left(h+s\right) + 2\left(h+s-z\right)\cot\theta, \tag{29}$$

$$\frac{\partial(h\bar{u})}{\partial x} + \frac{\partial(h\bar{v})}{\partial y} = 0, \tag{30}$$

where the over-bar denotes depth-averaged components of velocity, namely:

$$\bar{u} = \frac{1}{h}\int_s^f u dz, \quad \bar{v} = \frac{1}{h}\int_s^f v dz. \tag{31}$$

The problem is closed by specifying averaged inflow conditions and the assumption of fully developed flow both upstream and downstream, namely:

$$\bar{u}|_{x=0} = 2/3, \quad \bar{v}|_{x=0} = 0, \quad p|_{x=0} = 2\left(1-z\right)\cot\theta, \quad h|_{x=0} = 1, \tag{32}$$

$$\frac{\partial\left(\bar{u},\bar{v},p,h\right)}{\partial x}|_{x=l_p} = \frac{\partial\left(\bar{u},\bar{v},p,h\right)}{\partial y}|_{y=0,w_p} = 0. \tag{33}$$

Note that since topography appears as a function in the DAF equations, in the case of a trench topography having vertical sides equation (11) is replaced with one for which the sides are approximated via arctangent functions, [20], and takes the form:

$$s_{trench}\left(x^*,y^*\right) = -\frac{s_0}{4\tan^{-1}\frac{l_t}{2\delta}\tan^{-1}\frac{w_t}{2\delta}}\left[\tan^{-1}\left(\frac{x^*+l_t/2}{\delta}\right) - \tan^{-1}\left(\frac{x^*-l_t/2}{\delta}\right)\right]$$

$$\times \left[\tan^{-1} \left(\frac{y^* + w_t/2}{\delta} \right) - \tan^{-1} \left(\frac{y^* - w_t/2}{\delta} \right) \right], \tag{34}$$

with δ being a steepness factor, chosen so that the function approximates the vertical sides of the trench as closely as possible; a value of $\delta = 0.001$ is used in the present work as it is sufficient to produce no observable mesh dependency between the free-surface solutions generated.

The above DAF equations are solved on a rectangular computational domain $(x, y) \in \Omega = (0, l_p) \times (0, w_p)$, subdivided using a staggered arrangement of unknowns, consisting of n_x and n_y regular cells in the x and y directions respectively; the convective terms are discretised via a Total Variation Diminishing (TVD) scheme. The unknown variables, film thickness h, pressure p and velocity components $(\bar{u}, \bar{v})$ are located at cell centres (i, j) and cell faces $(i + 1/2, j)$, $(i, j + 1/2)$, respectively. An automatic adaptive time-stepping procedure which utilises estimates of the local truncation error to optimise the size of the time step and minimise computational cost is employed. At the solution stage of the temporal discretisation, the system of equations is solved using a customised multigrid strategy. The discretised equations are solved using a fixed number of Full Approximation Storage V-cycles on intermediate grid levels and up to 10 V-cycles on the first grid level so that residuals are reduced below a specified tolerance. Further details concerning the spatial and temporal discretisation schemes and the multigrid solution method can be found in [20].

Figures

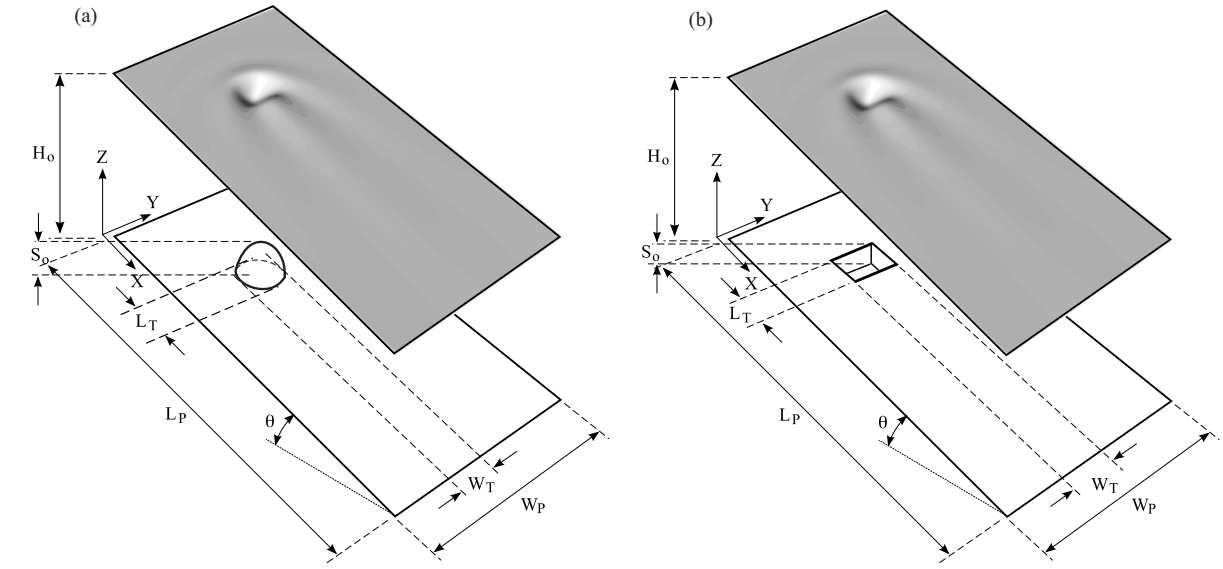

Figure 1: Schematic diagram of gravity-driven film flow over a planar substrate containing a well-defined (a) hemispheroid and (b) trench topography; showing the coordinate system adopted and surface geometry.

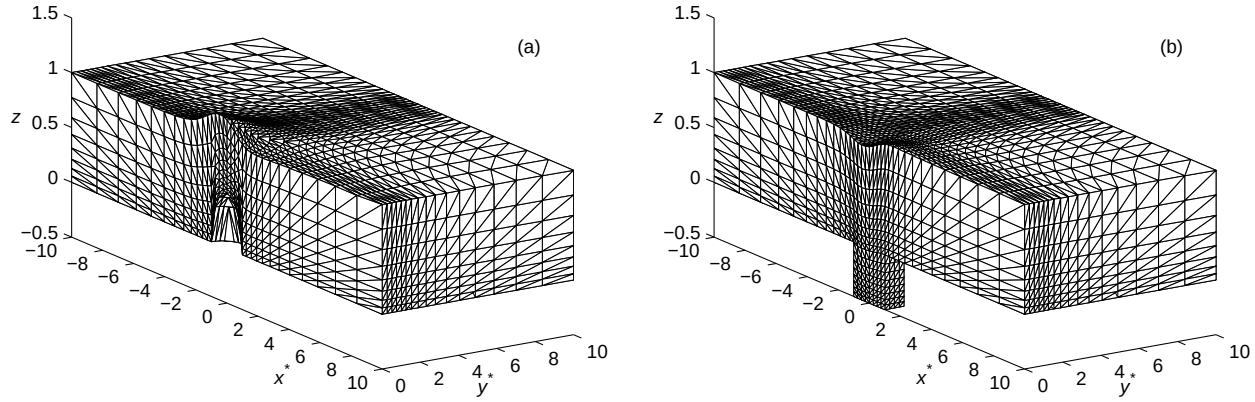

Figure 2: Typical irregular finite element grid structure comprised of tetrahedral elements for three-dimensional film flow over: (a) a hemispheroid obstacle; (b) a trench topography. In both cases $l_t = w_t = 2.0$ and $s_0 = 0.5$. For the particular grid structures shown the number of elements in the half solution domain is comprised of $6 \times 32 \times 16 \times 8$ (spanning the entire substrate for $s \geq 0$) and $6 \times 8 \times 4 \times 10$ additional elements (within the trench, $s < 0$).

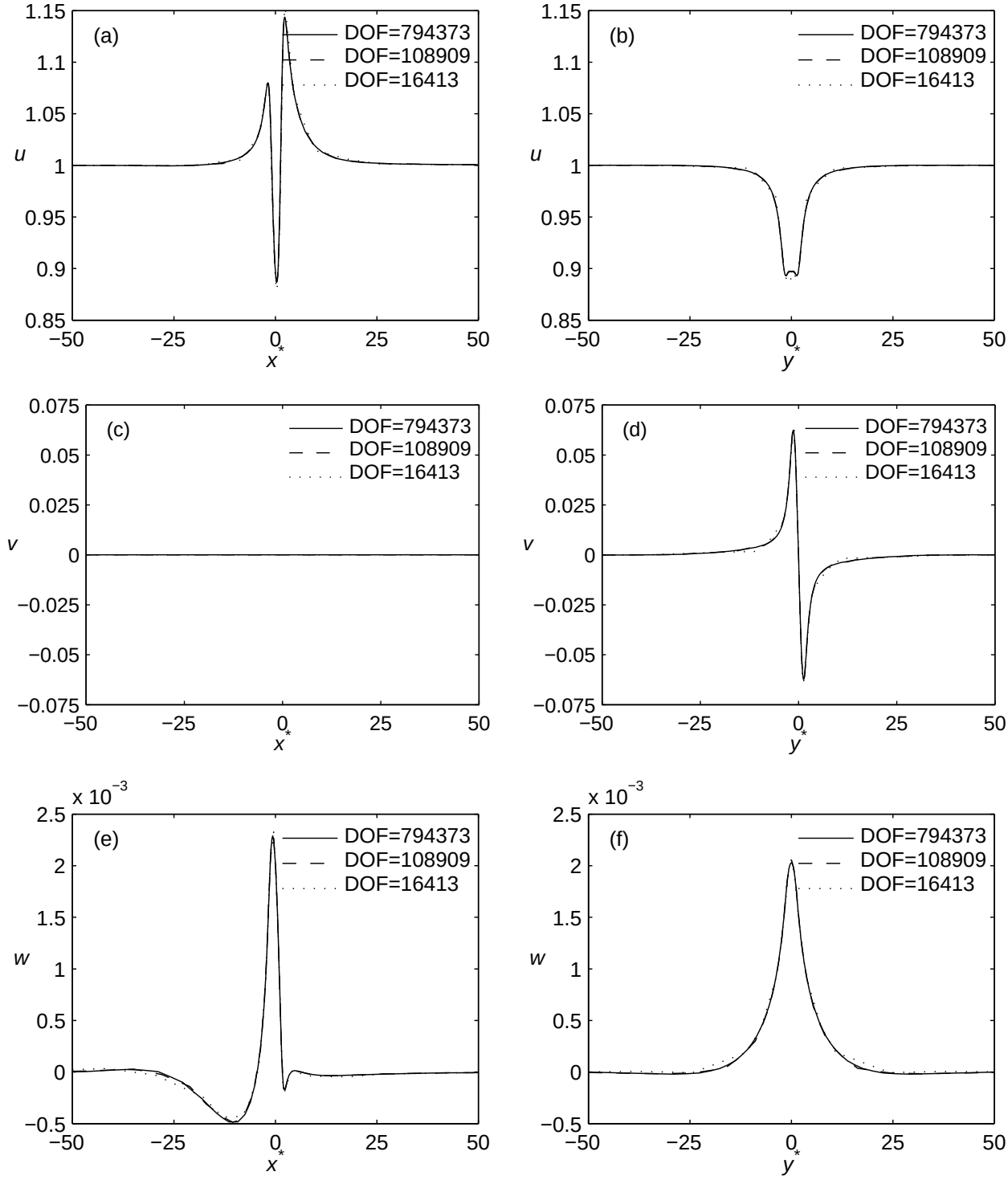

Figure 3: Grid-independency of N-S predicted components of velocity at the free surface, $z = f$. Streamwise (u), spanwise (v) and normal (w) velocity components through the centre of a trench topography with $l_t = w_t = 3$, $s_0 = 1.0$, Re $= 10$, Ca $= 0.001$ and $\theta = 7°$. Cases (a), (c) and (e) are in the streamwise direction with y^*=0; cases (b), (d) and (f) in the spanwise direction with x^*=0.

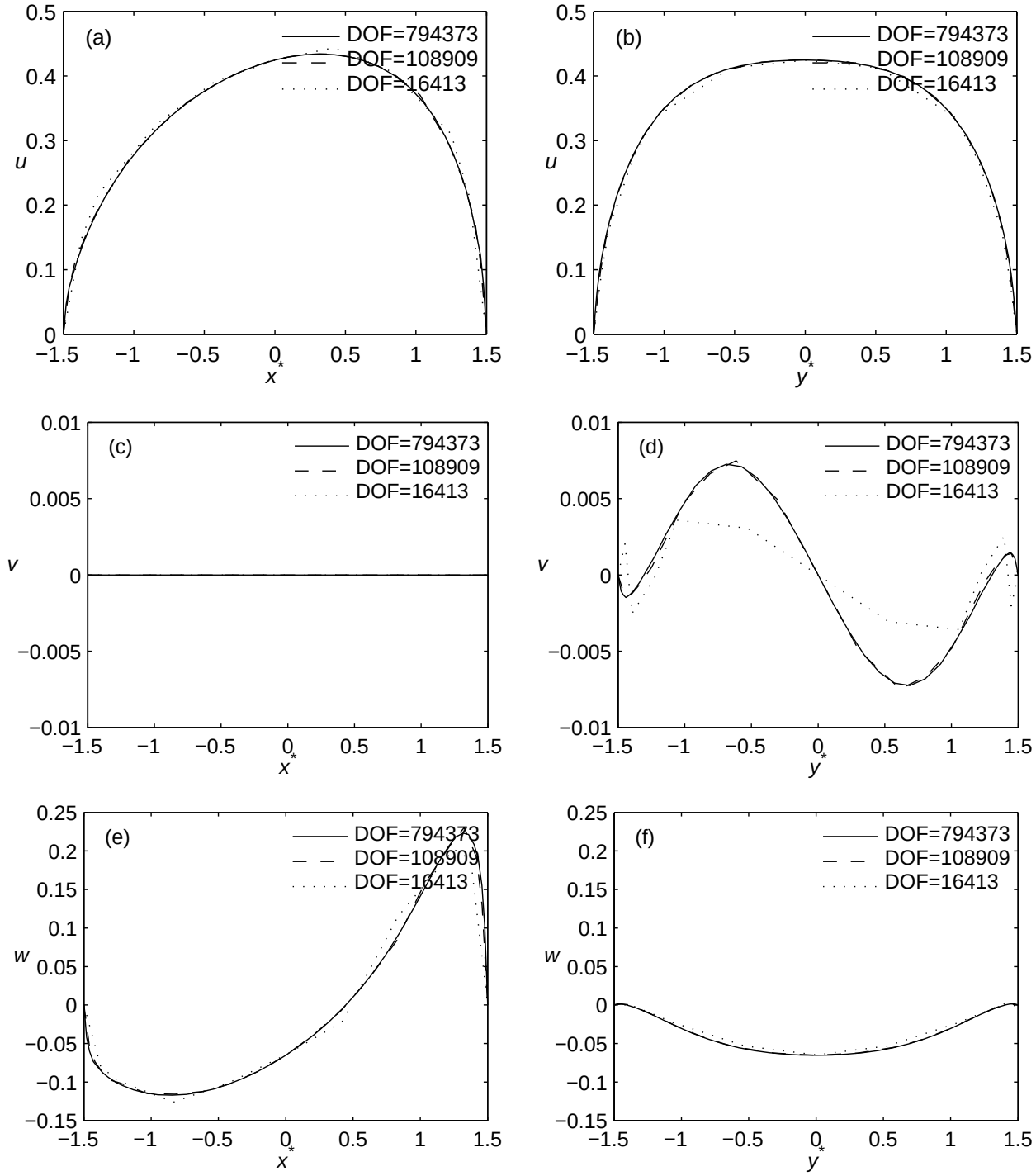

Figure 4: Grid-independency of N-S predicted components of velocity at the plane $z = 0$. Streamwise (u), spanwise (v) and normal (w) velocity components through the centre of a trench topography with $l_t = w_t = 3$, $s_0 = 1.0$, Re $= 10$, Ca $= 0.001$ and $\theta = 7°$. Cases (a), (c) and (e) are in the streamwise direction with y^*=0; cases (b), (d) and (f) in the spanwise direction with x^*=0.

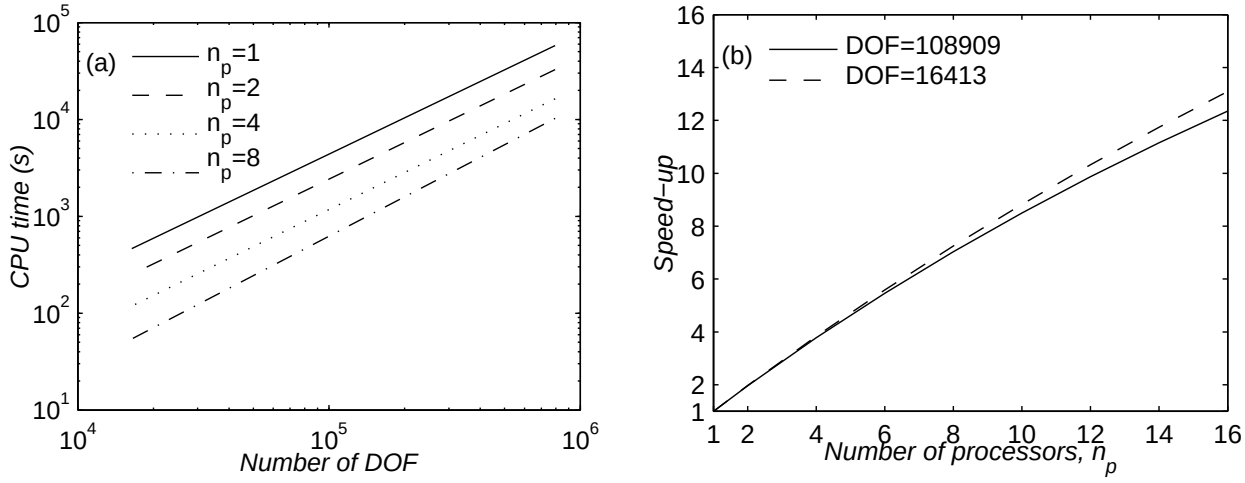

Figure 5: CPU time dependence on mesh density (left) and speed-up dependence on number of processors (right), taking flow over trench topography with $l_t = w_t = 3$, $s_0 = 1.0$, Re $= 10$, Ca $= 0.001$ and $\theta = 7^\circ$ as a benchmark.

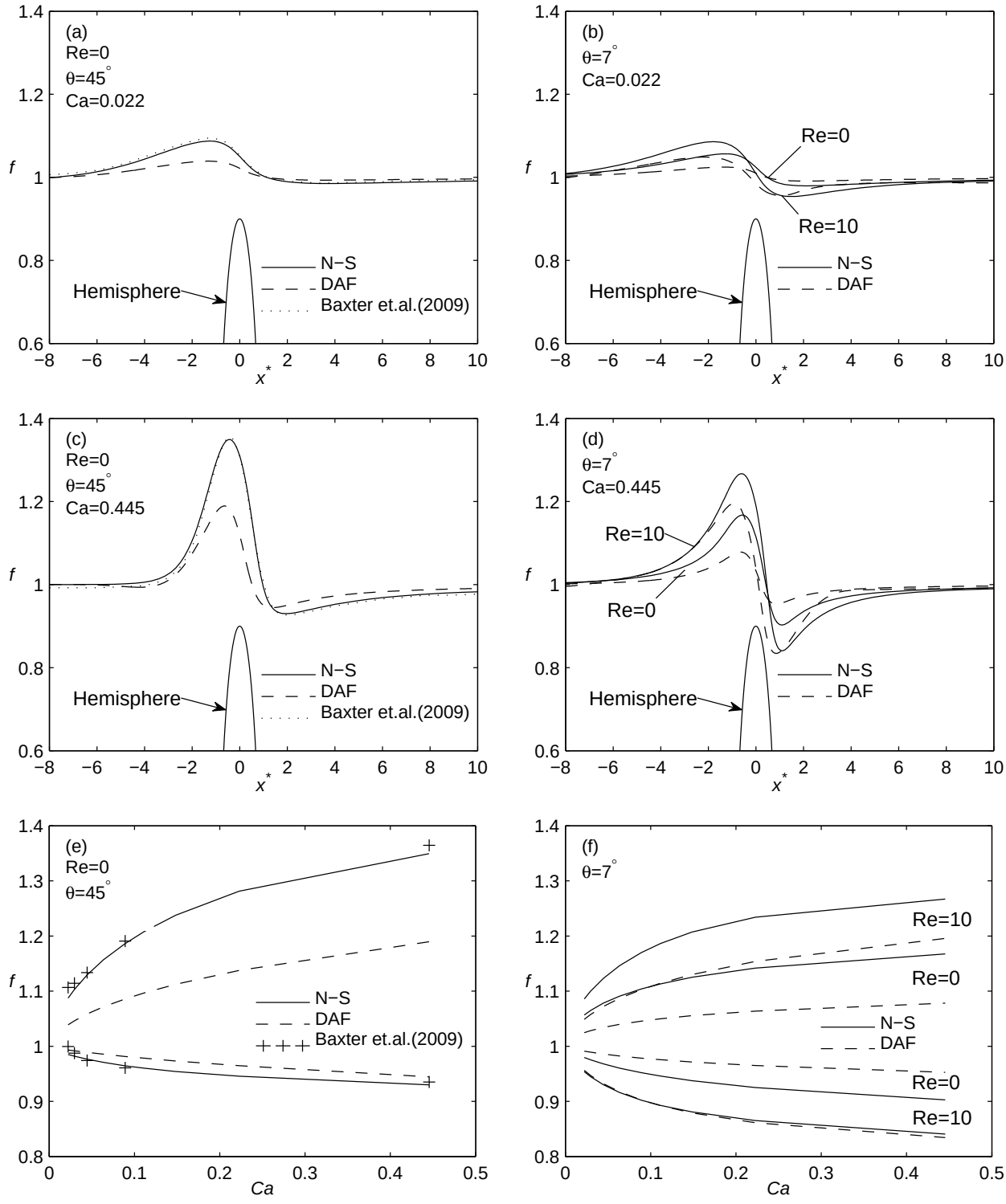

Figure 6: Comparison of results for the flow over a hemispheric obstacle with diameter $l_t = 1.8$: N-S, DAF and boundary element solutions for $\theta = 45°$, Re $= 0$ (left); N-S and DAF for $\theta = 7°$, Re $= 0$ and 10 (right); streamwise centreline free-surface profiles for Ca $= 0.022$ (top) and 0.445 (middle); maximum and minimum free-surface deflections for a range of Ca (bottom). The boundary element results are taken from Figures 15 and 16 of [25].

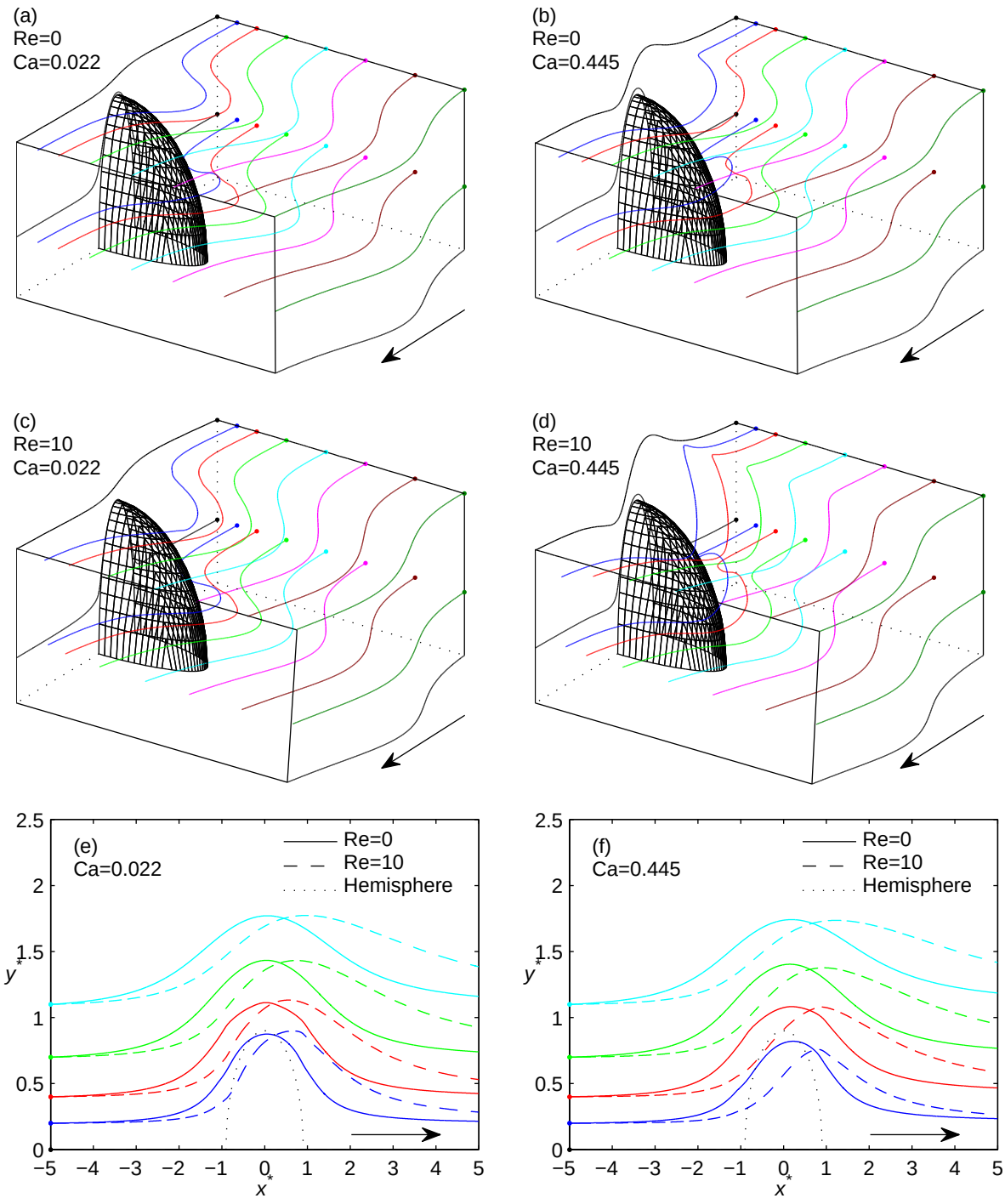

Figure 7: Flow patterns obtained by integrating along path lines, for film flow over a hemispheric obstacle with diameter $l_t = 1.8$ and $\theta = 7°$, the starting positions of which are at $z = 0.4$ and $z = f$ (the free surface) and denoted as filled in circles: Ca = 0.022 (left) and Ca = 0.445 (right); Re = 0 (top), Re = 10 (middle), at $z = f$ viewed from above (bottom) – the colours correspond to different trajectory starting points and the footprint of the obstacle, at $z = 0$, is represented as the dotted curve. The symmetry plane is on the left hand side (top and middle) and along the lower edge (bottom). The arrow shows the direction of flow.

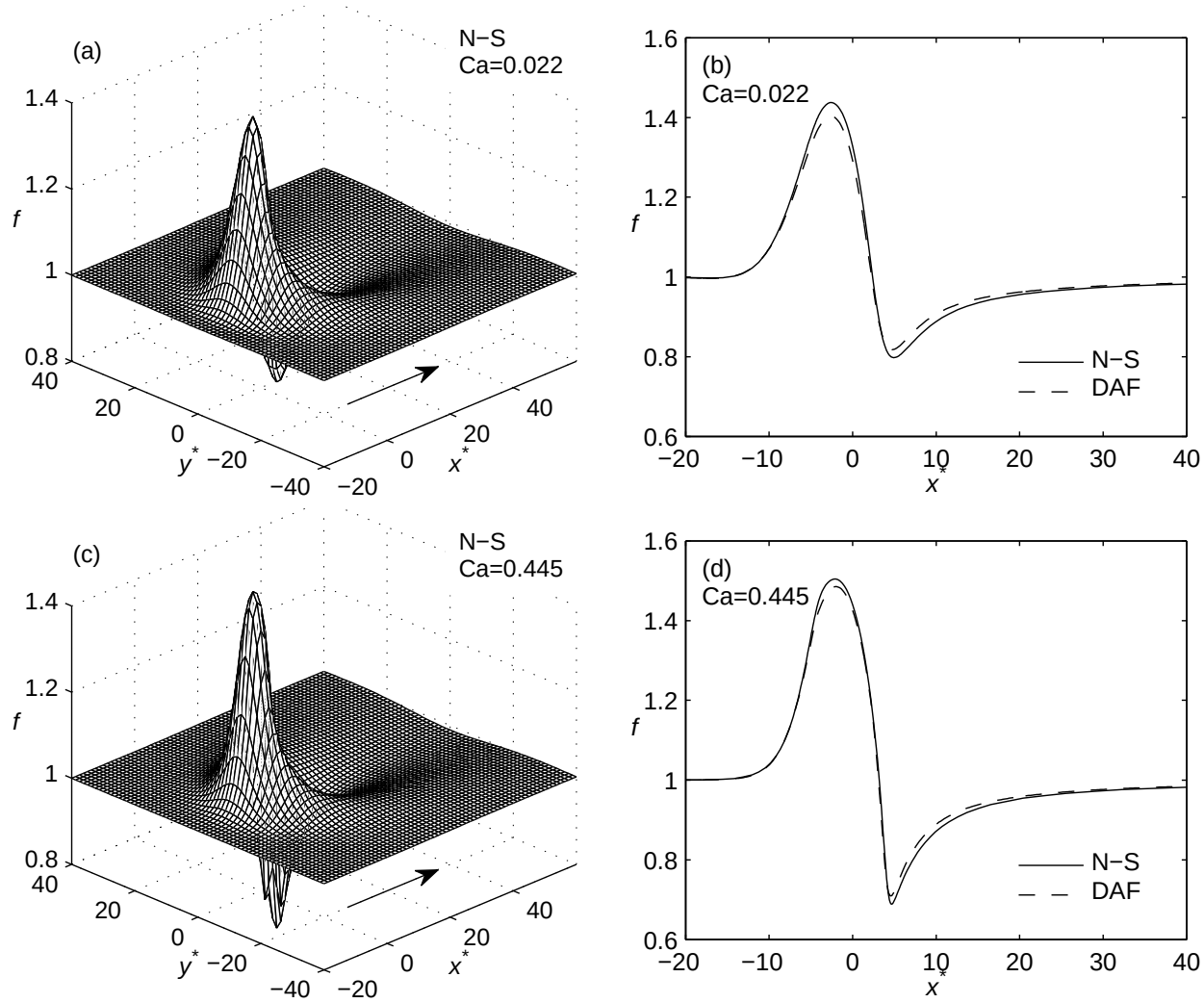

Figure 8: Comparison of the predicted (N-S and DAF) free-surface disturbance for flow over a hemispheroid obstacle with $l_t = w_t = 9$, $s_0 = 0.9$, Re $= 10$ and $\theta = 7°$. On left, N-S free-surface disturbance; on right comparison between N-S and DAF streamwise free-surface profiles at $y^* = 0$; Ca $= 0.022$ (top) and Ca $= 0.445$ (bottom). The arrow shows the direction of flow.

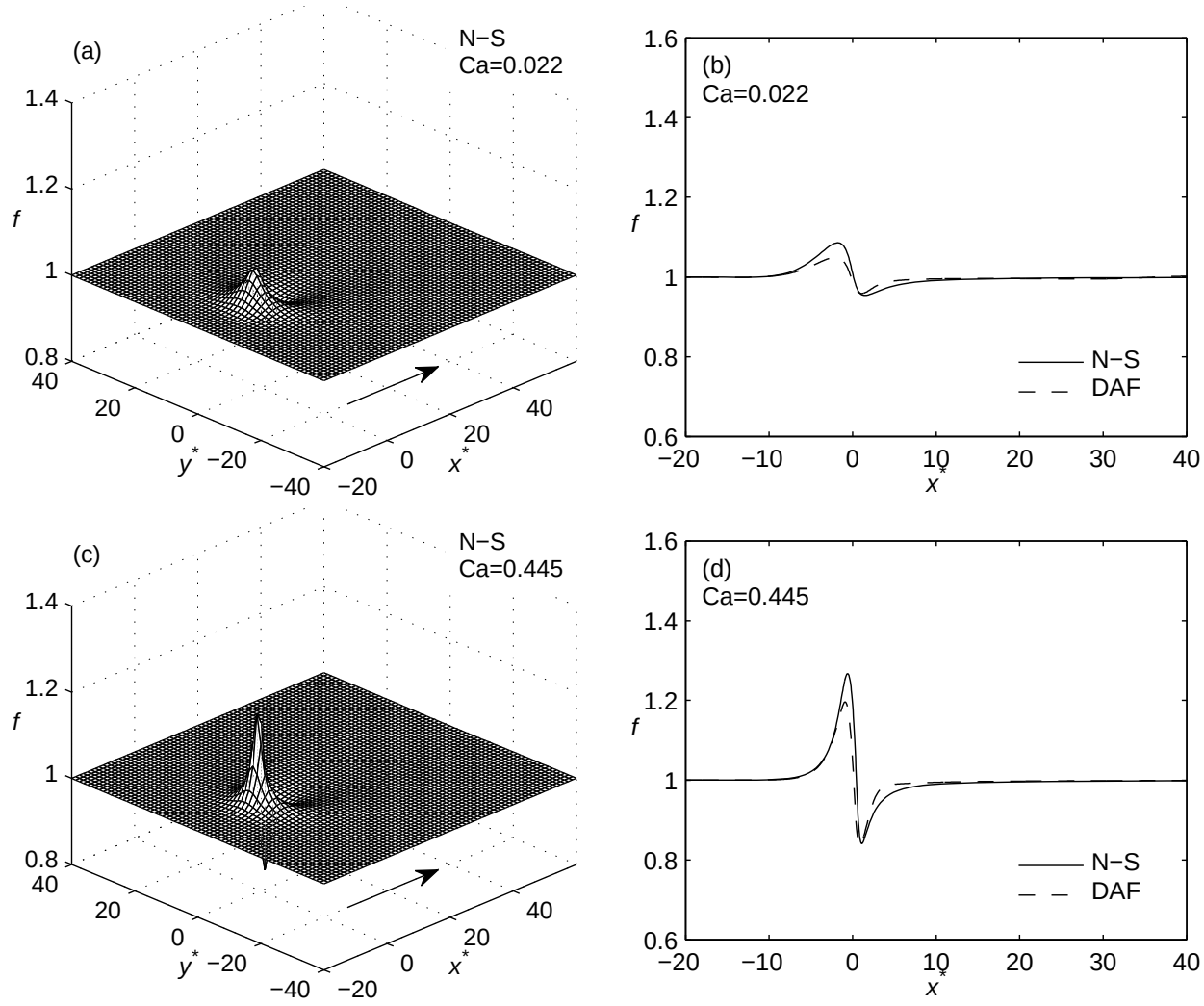

Figure 9: Comparison of the predicted (N-S and DAF) free-surface disturbance for flow over a hemispheric obstacle with $l_t = w_t = 1.8$, $s_0 = 0.9$, Re $= 10$ and $\theta = 7°$. On left, N-S free-surface disturbance and on right comparison between N-S and DAF streamwise free-surface profiles at $y^* = 0$; Ca $= 0.022$ (top) and Ca $= 0.445$ (bottom). The arrow shows the direction of flow.

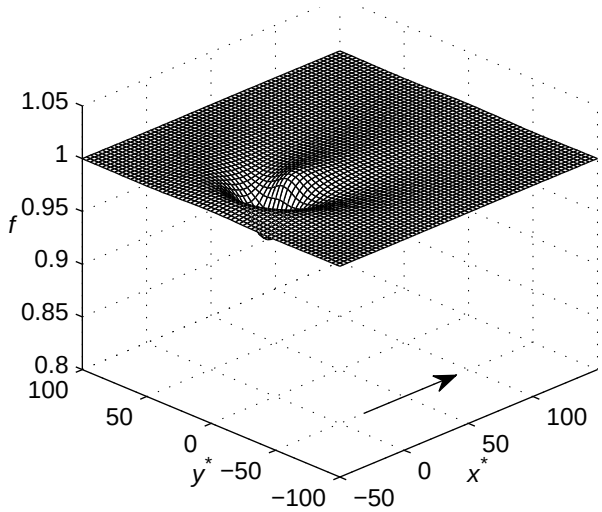

Figure 10: Predicted (N-S) free-surface disturbance for flow over a square trench topography, considered experimentally and presented in Figure 7 of [10], with $l_t = w_t = 12$, $s_0 = 0.25$, $\mathrm{Re} = 2.45$, $\mathrm{Ca} = 3.5 \cdot 10^{-4}$ and $\theta = 30°$. The arrow shows the direction of flow.

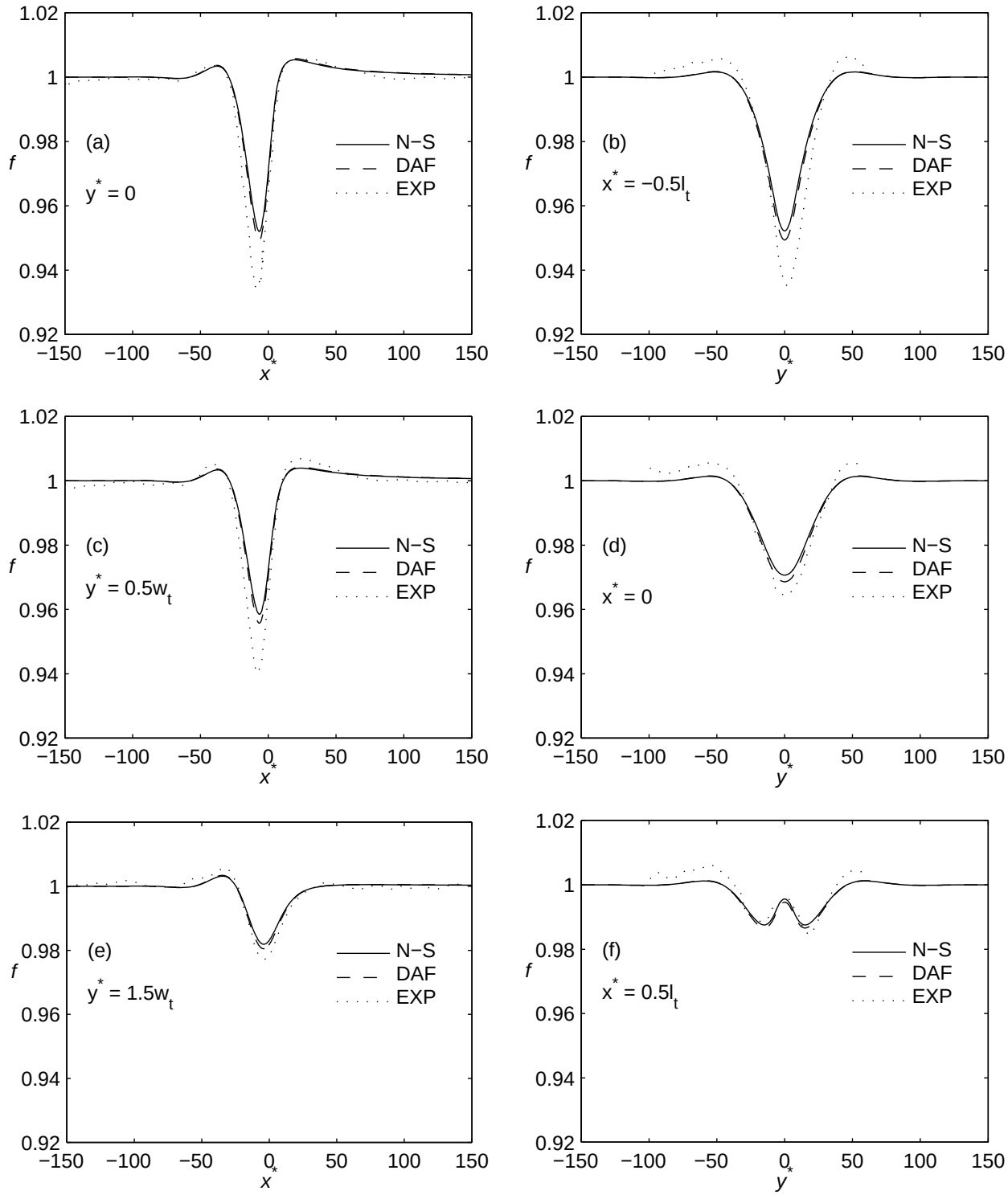

Figure 11: Comparison between predicted (N-S and DAF) and experimentally (EXP) obtained streamwise (left, Figure 8 of [10]) and spanwise (right, Figure 9 of [10]) free-surface profiles through the square trench of Figure 10 at different locations: (a) $y^* = 0$; (b) $x^* = -0.5l_t$; (c) $y^* = 0.5w_t$; (d) $x^* = 0$; (e) $y^* = 1.5w_t$; (f) $x^* = 0.5l_t$.

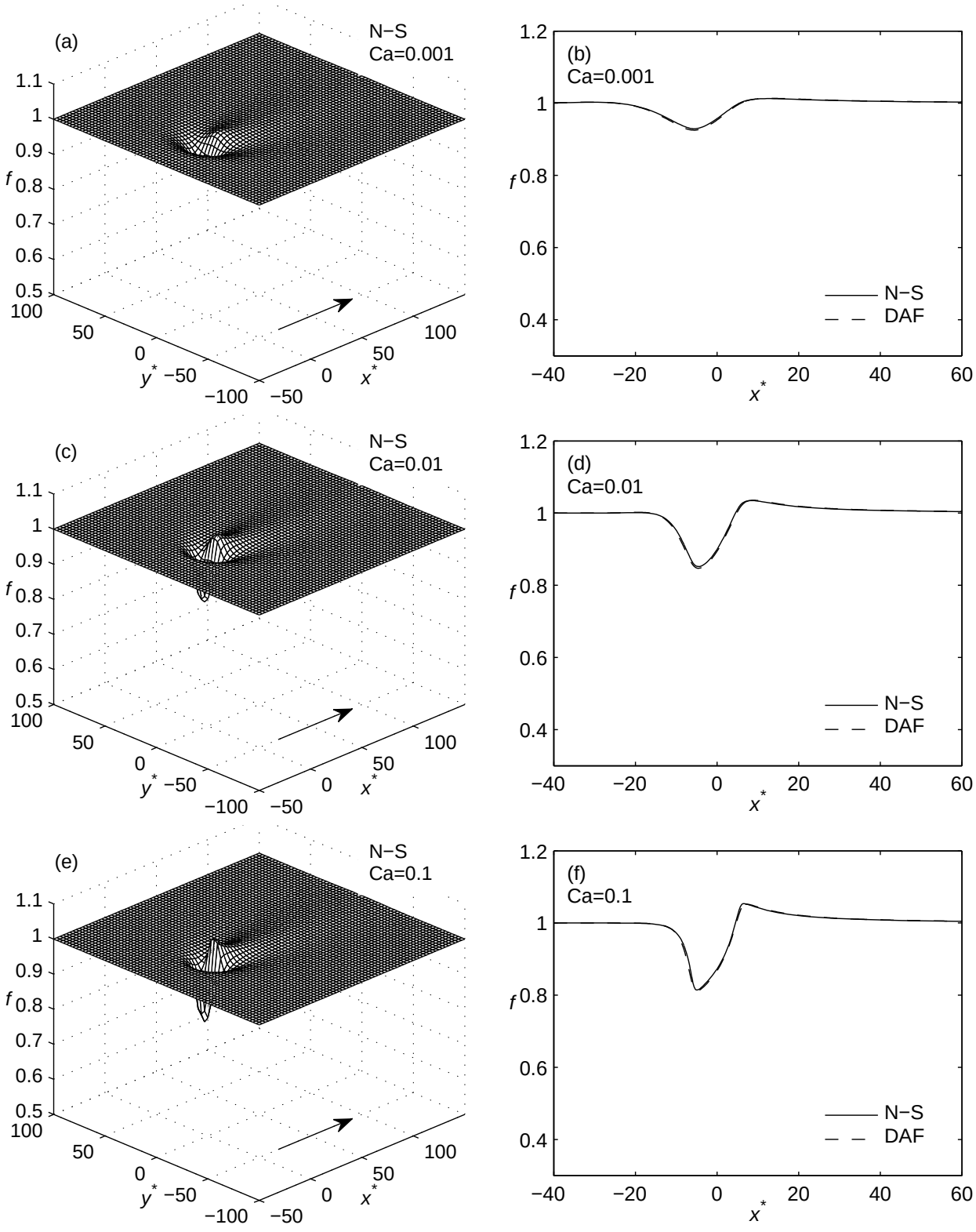

Figure 12: Comparison of the predicted (N-S and DAF) free-surface disturbance for flow over a square trench topography with $l_t = w_t = 12$, $s_0 = 0.25$, Re $= 0$ and $\theta = 7°$. On the left, N-S free-surface disturbance; on the right comparison between N-S and DAF streamwise free-surface profiles at $y^* = 0$; from top to bottom Ca $= 0.001$, 0.01 and 0.1. The arrow shows the direction of flow.

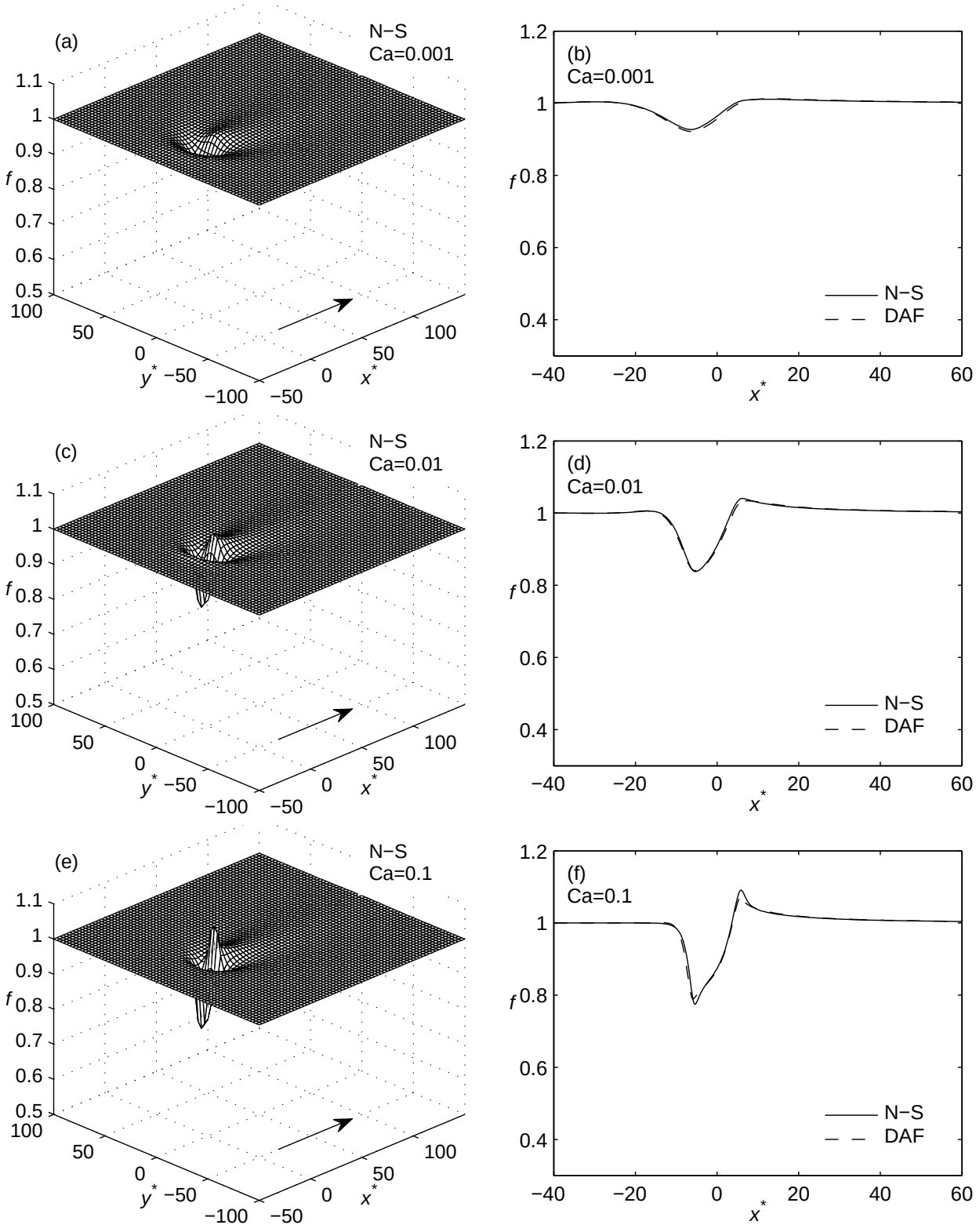

Figure 13: Comparison of the predicted (N-S and DAF) free-surface disturbance for flow over a square trench topography with $l_t = w_t = 12$, $s_0 = 0.25$, Re $= 10$ and $\theta = 7°$. On the left, N-S free-surface disturbance; on the right, comparison between N-S and DAF streamwise free-surface profiles at $y^* = 0$; from top to bottom Ca $= 0.001$, 0.01 and 0.1. The arrow shows the direction of flow.

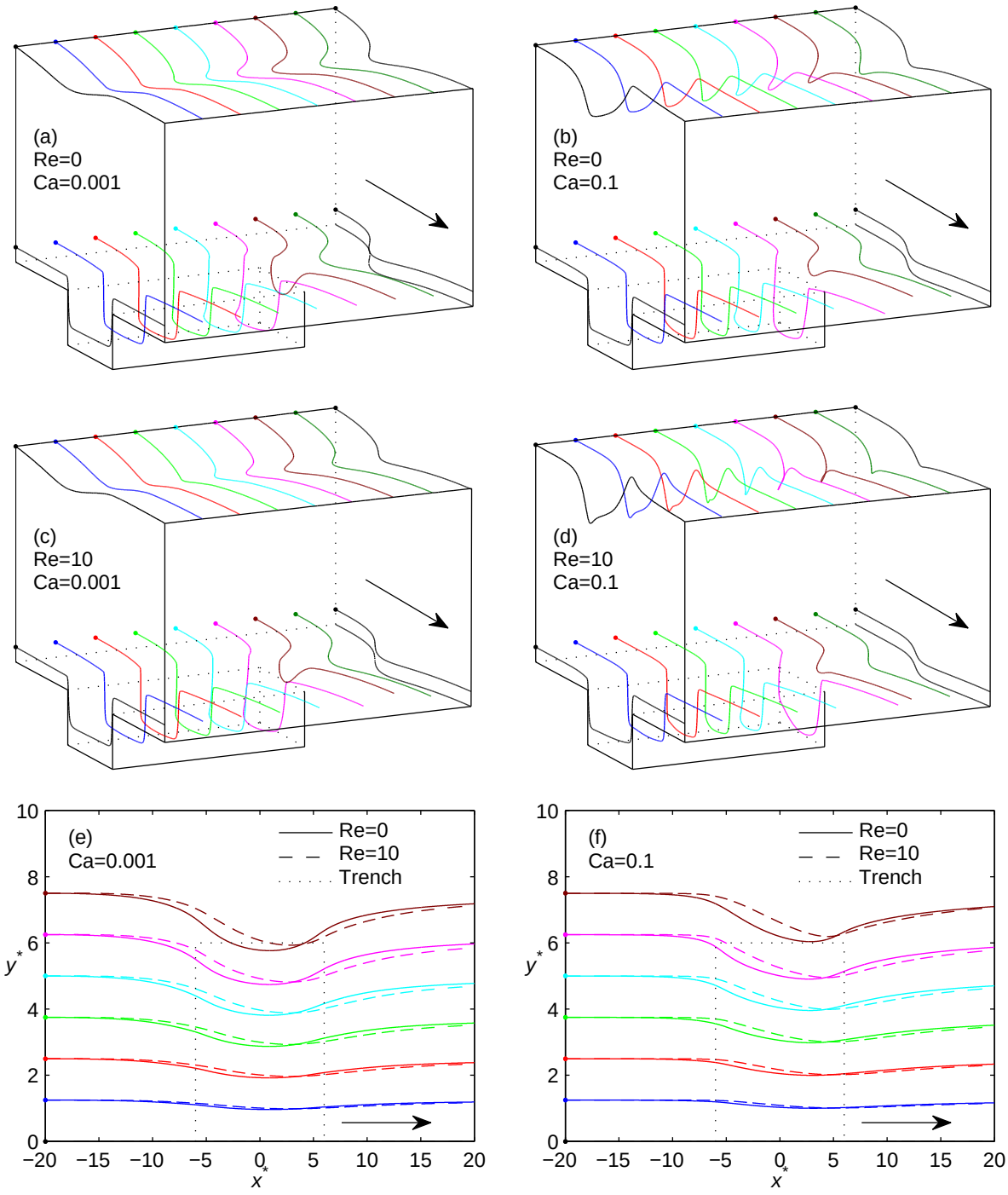

Figure 14: Flow patterns obtained by integrating along path lines,for film flow over a square trench topography with $l_t = w_t = 12$, $s_0 = 0.25$ and $\theta = 7°$, the starting positions of which are at $z = 0.05$ and $z = f$ (the free surface) and denoted as filled in circles: Ca $= 0.001$ (left) and Ca $= 0.1$ (right); Re $= 0$ (top), Re $= 10$ (middle), at $z = f$ viewed from above (bottom) – the colours correspond to different trajectory starting points and the edge of the trench, at $z = 0$, is represented by the dotted lines. The symmetry plane is on the left hand side (top and middle) and along the lower edge (bottom). The arrow shows the direction of flow.

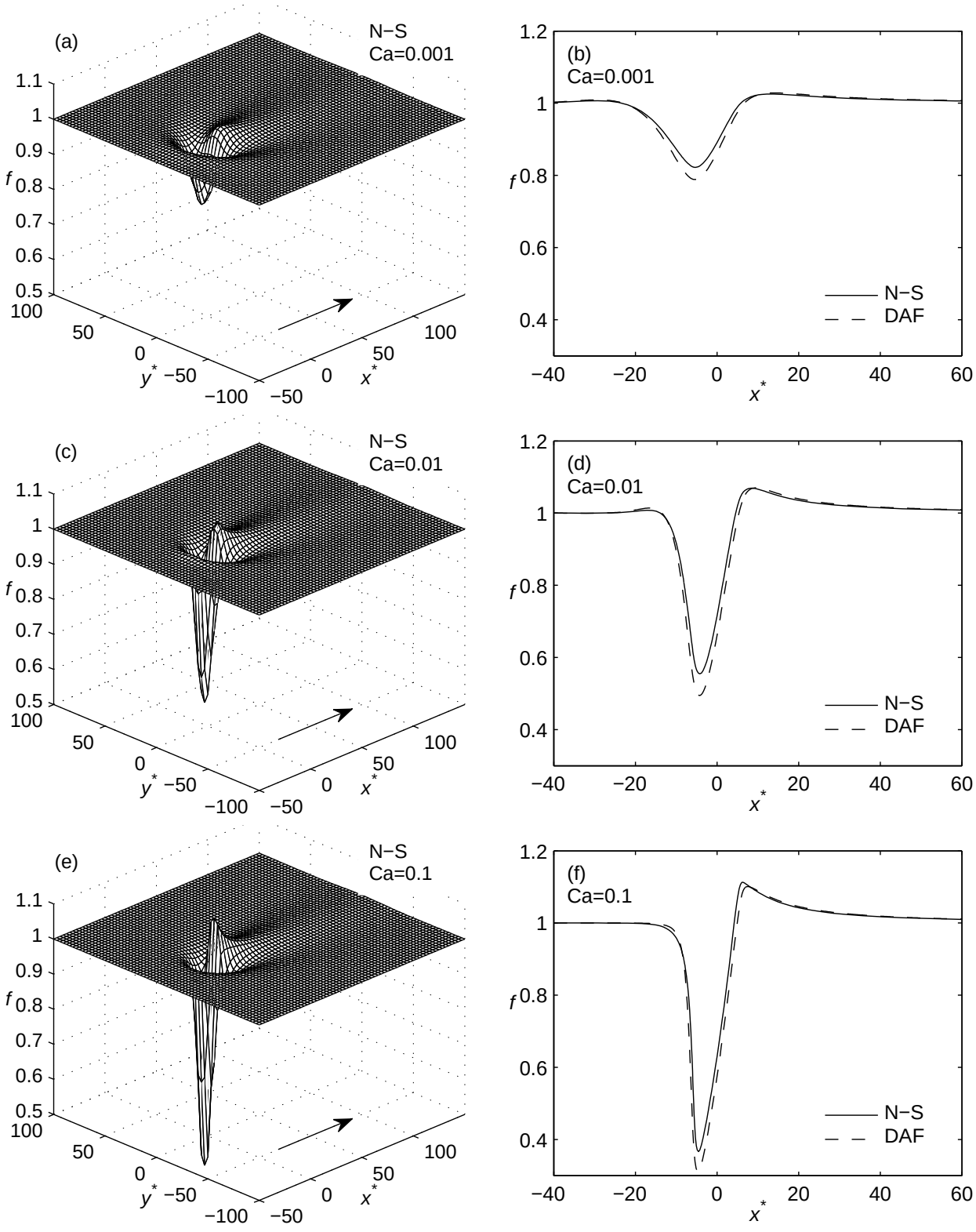

Figure 15: Comparison of the predicted (N-S and DAF) free-surface disturbance for flow over a square trench topography with $l_t = w_t = 12$, $s_0 = 1.0$, Re $= 0$ and $\theta = 7°$. On the left, N-S free-surface disturbance; on the right comparison between N-S and DAF streamwise free-surface profiles at $y^* = 0$; from top to bottom Ca $= 0.001$, 0.01 and 0.1. The arrow shows the direction of flow.

References

[1] R. Craster, O. Matar, Dynamics and stability of thin liquid films., Rev. Mod. Phys. 81 (3) (2009) 1131–1198.

[2] D. Walters, Disguising the leaf surface: the use of leaf coatings for plant disease control., Eur. J. Plant Pathol. 114 (3) (2006) 255–260.

[3] D. Gaver, J. Grotberg, The dynamics of a localized surfactant on a thin-film., J. Fluid Mech. 213 (1990) 127–148.

[4] S. Kistler, P. Schweizer (Eds.), Liquid Film Coating, Chapman and Hall, 1997.

[5] K. Helbig, A. Alexeev, T. Gambaryan-Roisman, P. Stephan, Evaporation of falling and shear-driven thin films on smooth and grooved surfaces., Flow Turbul. Combust. 75 (1-4) (2005) 85–104.

[6] K. Helbig, R. Nasarek, T. Gambaryan-Roisman, P. Stephan, Effect of longitudinal mini-grooves on flow stability and wave characteristics of falling liquid films., J. Heat Trans.-T. ASME 131 (1) (2009) 011601.

[7] N. Linn, C.-H. Sun, P. Jiang, B. Jiang, Self-assembled biomimetic antireflection coatings., Appl. Phys. Lett. 91 (10).

[8] M. Budakli, T. Gambaryan-Roisman, P. Stephan, Influence of surface topography on heat transfer in shear-driven liquid films., J. Phys.: Conf. Ser. 395 (2012) 012164.

[9] J. Lewis, Direct ink writing of 3d functional materials., Adv. Funct. Mat. 16 (17) (2006) 2193–2204.

[10] M. Decré, J. Baret, Gravity-driven flows of viscous liquids over two-dimensional topographies., J. Fluid Mech. 487 (2003) 147–166.

[11] L. Stillwagon, R. Larson, Fundamentals of topographic substrate leveling., J. Appl. Phys. 63 (11) (1988) 5251–5258.

[12] L. Stillwagon, R. Larson, Leveling of thin-films over uneven substrates during spin coating., Phys. Fluids A 2 (11) (1990) 1937–1944.

[13] V. Bontozoglou, K. Serifi, Falling film flow along steep two-dimensional topography: The effect of inertia., Int. J. Multiphas. Flow 34 (8) (2008) 734–747.

[14] C. Heining, T. Pollak, N. Aksel, Pattern formation and mixing in three-dimensional film flow., Phys. Fluids 24 (4).

[15] N. Cowling, P. Gaskell, Y. Lee, H. Thompson, Towards the efficient numerical solution of three-dimensional thin film flows on real surfaces: an evaluation of finite-difference-based schemes., Proc. I. Mech. E. part C, J. Mech. Sci. 225 (C8) (2011) 1886–1902.

[16] P. Gaskell, P. Jimack, M. Sellier, H. Thompson, Flow of evaporating, gravity-driven thin liquid films over topography., Phys. Fluids 18 (1) (2006) 013601.

[17] L. Schwartz, R. Roy, R. Eley, H. Princen, Surfactant-driven motion and splitting of droplets on a substrate., J. Eng. Math. 50 (2-3) (2004) 157–175.

[18] S. Veremieiev, H. Thompson, M. Scholle, Y. Lee, P. Gaskell, Electrified thin film flow at finite Reynolds number on planar substrates featuring topography., Int. J. Multiphas. Flow 44 (2012) 48–69.

[19] D. Slade, S. Veremieiev, Y. Lee, P. Gaskell, Gravity-driven thin film flow: The influence of topography and surface tension gradient on rivulet formation., Chem. Eng. Process.: Process Intens. 68 (2013) 7–12.

[20] S. Veremieiev, H. Thompson, Y. Lee, P. Gaskell, Comput. Fluids 39 (3) (2010) 431–450.

[21] A. Wierschem, C. Lepski, N. Aksel, Effect of long undulated bottoms on thin gravity-driven films., Acta Mech. 179 (1-2) (2005) 41–66.

[22] K. Argyriadi, M. Vlachogiannis, V. Bontozoglou, Experimental study of inclined film flow along periodic corrugations: The effect of wall steepness., Phys. Fluids 18 (1) (2006) 15.

[23] C. Pozrikidis, S. Thoroddsen, The deformation of a liquid-film flowing down an inclined plane wall over a small particle arrested on the wall., Phys. Fluids A 3 (11) (1991) 2546–2558.

[24] M. Blyth, C. Pozrikidis, Film flow down an inclined plane over a three-dimensional obstacle., Phys. Fluids 18 (5) (2006) 052104.

[25] S. Baxter, H. Power, K. Cliffe, S. Hibberd, Three-dimensional thin film flow over and around an obstacle on an inclined plane., Phys. Fluids 21 (3) (2009) 032102.

[26] S. Baxter, H. Power, K. Cliffe, S. Hibberd, Free surface Stokes flows obstructed by multiple obstacles., Int. J. Num. Meth. Fl. 62 (5) (2010) 530–564.

[27] J. Sprittles, Y. Shikhmurzaev, Finite element simulation of dynamic wetting flows as an interface formation process., J. Comput. Phys. 233 (2013) 34–65.

[28] J. Spurk, N. Aksel, Fluid Mechanics, 2nd Edition, Academic Press, Springer, 2008.

[29] L. Landau, E. Lifshitz, Fluid Mechanics, 2nd Edition, Pergamon, Oxford, 1987.

[30] P. Hood, C. Taylor, Navier-Stokes equations using mixed interpolation., in: J. Oden, O. Zienkiewicz, R. Gallagher, C. Taylor (Eds.), Finite Element Method in Flow Problems, UAH Press, Huntsville, 1974, pp. 121–132.

[31] O. Ladyzhenskaya, The Mathematical Theory of Viscous Incompressible Flow, 2nd Edition, Gordon and Breach, New York, 1963.

[32] I. Babuška, Error-bounds for finite element method., Numerische Mathematik 16 (4) (1971) 322–333.

[33] F. Brezzi, On the existence, uniqueness and approximation of saddle-point problems arising from lagrangian multipliers., Revue Francaise D Automatique Informatique Recherche Operationnelle 8 (NR2) (1974) 129–151.

[34] K. Christodoulou, S. Kistler, P. Schunk, Advances in computational methods for free surface flows., in: S. Kistler, P. Schweizer (Eds.), Liquid Film Coating, Chapman and Hall, 1997, pp. 297–366.

[35] R. Cairncross, P. Schunk, T. Baer, R. Rao, P. Sackinger, A finite element method for free surface flows of incompressible fluids in three dimensions. Part I. Boundary fitted mesh motion., Int. J. Num. Meth. Fl. 33 (3) (2000) 375–403.

[36] T. Baer, R. Cairncross, P. Schunk, R. Rao, P. Sackinger, A finite element method for free surface flows of incompressible fluids in three dimensions. Part II. Dynamic wetting lines., Int. J. Num. Meth. Fl. 33 (3) (2000) 405–427.

[37] R. Fosdick, H. Tang, Surface transport in continuum mechanics., Math. Mech. Solids 14 (6) (2009) 587–598.

[38] S. Kistler, L. Scriven, Coating flows., in: J. Pearson, S. Richardson (Eds.), Computational Analysis of Polymer Processing, Elsevier Applied Science, London, 1983, Ch. 8, pp. 243–299.

[39] J. Reddy, D. Gartling, The Finite Element Method in Heat Transfer and Fluid Dynamics, Second Edition, 2nd Edition, Taylor & Francis, 2000.

[40] S. Veremieiev, Gravity-driven continuous thin film flow over topography., Ph.D. thesis, University of Leeds (2011).

[41] T. Chung, Computational Fluid Dynamics, Cambridge University Press, Cambridge, 2002.

[42] I. Duff, J. Reid, The multifrontal solution of indefinite sparse symmetric linear equations., Acm T. Math. Software 9 (3) (1983) 302–325.

[43] I. Duff, J. Reid, The multifrontal solution of unsymmetric sets of linear equations., SIAM J. Sci. Comput. 5 (3) (1984) 633–641.

[44] M. Snir, S. Otto, S. Huss-Lederman, D. Walker, J. Dongarra, MPI: The Complete Reference, The MIT Press, Cambridge, Massachusetts, 1996.

[45] J. Dongarra, J. Du Cruz, S. Hammerling, I. Duff, Algorithm 679: A set of level 3 basic linear algebra subprograms: model implementation and test programs., Acm T. Math. Software 16 (1) (1990) 18–28.

[46] L. Blackford, J. Choi, A. Cleary, E. D'Azevedo, J. Demmel, I. Dhillon, J. Dongarra, S. Hammarling, G. Henry, A. Petitet, K. Stanley, D. Walker, R. Whaley, ScaLAPACK Users' Guide, SIAM, 1997.

[47] J. Liu, The multifrontal method for sparse matrix solution: Theory and practice., SIAM Rev. 34 (1) (1992) 82–109.

[48] P. Amestoy, I. Duff, J.-Y. L'Excellent, Multifrontal parallel distributed symmetric and unsymmetric solvers., Comp. Meth. Appl. Mech. Engrg. 184 (2-4) (2000) 501–520.

[49] P. Amestoy, I. Duff, J.-Y. L'Excellent, J. Koster, A fully asynchronous multifrontal solver using distributed dynamic scheduling., SIAM J. Matr Anal. Appl. 23 (1) (2001) 15–41.

[50] P. Amestoy, A. Guermouche, J.-Y. L'Excellent, S. Pralet, Hybrid scheduling for the parallel solution of linear systems., Parallel Comput. 32 (2) (2006) 136–156.

[51] J. Liu, The role of elimination trees in sparse factorization., SIAM J. Matr Anal. Appl. 11 (1) (1990) 134–172.

[52] G. Karypis, V. Kumar, METIS: A software package for partitioning unstructured graphs, partitioning meshes, and computing fill-reducing orderings of sparse matrices., Tech. rep., University of Minnesota, Minneapolis, MN (1998).

[53] G. Karypis, K. Schloegel, V. Kumar, PARMETIS: Parallel graph partitioning and sparse matrix ordering library., Tech. rep., University of Minnesota, Minneapolis, MN (2003).

[54] E. Agullo, A. Guermouche, J.-Y. L'Excellent, A parallel out-of-core multifrontal method: Storage of factors on disk and analysis of models for an out-of-core active memory., Parallel Comput. 34 (6-8) (2008) 296–317.

[55] H. Chang, Wave evolution on a falling film., Annu. Rev. Fluid Mech. 26 (1994) 103–136.

[56] J. Liu, J. Paul, J. Gollub, Measurements of the primary instabilities of film flows., J. Fluid Mech. 250 (1993) 69–101.

[57] J. Liu, J. Gollub, Solitary wave dynamics of film flows., Phys. Fluids 6 (5) (1994) 1702–1712.

[58] T. Benjamin, Wave formation in laminar flow down an inclined plane., J. Fluid Mech. 2 (6) (1957) 554–574.

[59] C. Yih, Stability of liquid flow down an inclined plane., Phys. Fluids 6 (3) (1963) 321–334.

[60] A. Wierschem, M. Scholle, N. Aksel, Vortices in film flow over strongly undulated bottom profiles at low Reynolds numbers., Phys. Fluids 15 (2) (2003) 426–435.

[61] S. Wang, X. Li, J. Xia, Y. Situ, M. De Hoop, Efficient scalable algorithms for solving dense linear systems with hierarchically semiseparable structures., SIAM J. Sci. Comput. 35 (6) (2013) C519–C544.

[62] V. Shkadov, Wave flow regimes of a thin layer of viscous fluid subject to gravity., Izv. Akad. Nauk SSSR Fluid Dynamics 2 (1) (1967) 29–34.

[63] V. Shkadov, Wave-flow theory for a thin viscous liquid layer., Izv. Akad. Nauk SSSR Fluid Dynamics 3 (2) (1968) 12–15.

[64] S. Saprykin, P. Trevelyan, R. Koopmans, S. Kalliadasis, Free-surface thin-film flows over uniformly heated topography., Phys. Rev. E 75 (2).

[65] S. Veremieiev, H. Thompson, Y. Lee, P. Gaskell, Chem. Eng. Process.: Process Intens. 50 (5-6) (2011) 537–542.

[66] P. Gaskell, P. Jimack, M. Sellier, H. Thompson, M. Wilson, Gravity-driven flow of continuous thin liquid films on non-porous substrates with topography., J. Fluid Mech. 509 (2004) 253–280.

[67] A. Mazouchi, G. Homsy, Free surface Stokes flow over topography., Phys. Fluids 13 (10) (2001) 2751–2761.

[68] J. Higdon, Stokes flow in arbitrary two-dimensional domains: shear flow over ridges and cavities., J. Fluid Mech. 159 (OCT) (1985) 195–226.

[69] R. Oliveira, Understanding adhesion: A means for preventing fouling., Exp. Thermal Fluid Sci. 14 (4) (1997) 316–322.

[70] M. Scholle, A. Haas, N. Aksel, M. Wilson, H. Thompson, P. Gaskell, Competing geometric and inertial effects on local flow structure in thick gravity-driven fluid films., Phys. Fluids 20 (12) (2008) 123101.